12-15-2022

Uncertainty of ICESat-2 ATL06- and ATL08-Derived Snow Depths for Glacierized and Vegetated Mountain Regions

Ellyn M. Enderlin
Boise State University

Colten M. Elkin
Boise State University

Madeline Gendreau
Boise State University

H.P. Marshall
Boise State University

Shad O'Neel
Boise State University

See next page for additional authors

Publication Information

Enderlin, Ellyn M.; Elkin, Colten M.; Gendreau, Madeline; Marshall, H.P.; O'Neel, Shad; McNeil, Christopher; Florentine, Caitlyn; and Sass, Louis. (2022). "Uncertainty of ICESat-2 ATL06- and ATL08-Derived Snow Depths for Glacierized and Vegetated Mountain Regions". *Remote Sensing of Environment, 283*, 113307. https://doi.org/10.1016/j.rse.2022.113307

Authors

Ellyn M. Enderlin, Colten M. Elkin, Madeline Gendreau, H.P. Marshall, Shad O'Neel, Christopher McNeil, Caitlyn Florentine, and Louis Sass

Remote Sensing of Environment 283 (2022) 113307

Contents lists available at ScienceDirect

Remote Sensing of Environment

journal homepage: www.elsevier.com/locate/rse

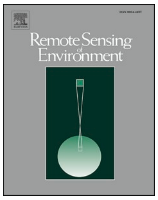

Uncertainty of ICESat-2 ATL06- and ATL08-derived snow depths for glacierized and vegetated mountain regions

Ellyn M. Enderlin [a,*], Colten M. Elkin [a], Madeline Gendreau [a], H.P. Marshall [a], Shad O'Neel [a,b], Christopher McNeil [c], Caitlyn Florentine [d], Louis Sass [c]

[a] *Boise State University Department of Geosciences, 1910 W University Drive, Boise, ID 83703; United States of America*
[b] *United States Army Corps of Engineers Cold Regions Research and Engineering Laboratory, 72 Lyme Rd, Hanover, NH 03755, United States of America*
[c] *United States Geological Survey, Alaska Science Center, 4210 University Drive, Anchorage, AK 99508, United States of America*
[d] *United States Geological Survey, Northern Rocky Mountain Science Cente, 169 Mather Drive, West, Glacier, MT 59936, United States of America*

ARTICLE INFO

Edited by Dr. Menghua Wang

Keywords:
ICESat-2
ATL06
ATL08
LiDAR
Snow
Vegetation
Glacier
Terrain
Validation

ABSTRACT

Seasonal snow melt dominates the hydrologic budget across a large portion of the globe. Snow accumulation and melt vary over a broad range of spatial scales, preventing accurate extrapolation of sparse in situ observations to watershed scales. The lidar onboard the Ice, Cloud, and land Elevation, Satellite (ICESat-2) was designed for precise mapping of ice sheets and sea ice, and here we assess the feasibility of snow depth-mapping using ICESat-2 data in more complex and rugged mountain landscapes. We explore the utility of ATL08 Land and Vegetation Height and ATL06 Land Ice Height differencing from reference elevation datasets in two end member study sites. We analyze ~3 years of data for Reynolds Creek Experimental Watershed in Idaho's Owyhee Mountains and Wolverine Glacier in southcentral Alaska's Kenai Mountains. Our analysis reveals decimeter-scale uncertainties in derived snow depth and glacier mass balance at the watershed scale. Both accuracy and precision decrease as slope increases: the magnitudes of the median and median of the absolute deviation of elevation errors (MAD) vary from ~0.2 m for slopes <5° to >1 m for slopes >20°. For glacierized regions, failure to account for intra- and inter-annual evolution of glacier surface elevations can strongly bias ATL06 elevations, resulting in underestimation of the mass balance gradient with elevation. Based on these results, we conclude that ATL08 and ATL06 observations are best suited for characterization of watershed-scale snow depth and mass balance gradients over relatively shallow slopes with thick snowpacks. In these regions, ICESat-2 elevation residual-derived snow depth and mass balance transects can provide valuable watershed scale constraints on terrain parameter- and model-derived estimates of snow accumulation and melt.

1. Introduction

Seasonal snow accumulation and melt represent an important component of mountain environments and downstream hydrologic systems (Viviroli et al., 2007). Mountain snow dominates the hydrologic budget across a large portion of the globe and, therefore, exerts a strong control on water resources for billions of people (Barnett et al., 2005). Changes in seasonal snow both directly and indirectly influence water resources. Decreased winter snow accumulation results in a net decrease in water availability downstream and changes in timing of water availability, particularly in summer months (e.g., Elias et al., 2021). Changes in seasonal snow can also have much longer-term indirect effects on water resources through alteration of local vegetation and glacier mass balance (Beniston, 2003; Freeman et al., 2018; Huss et al., 2017; Huss and Hock, 2018; Steinbauer et al., 2018; Wrzesien et al., 2018).

Despite the broad importance of snow, estimates of seasonal snow depth and the corresponding mass of water contained in the snowpack (i.e., snow water equivalent) at watershed to continent scales are highly uncertain (Dozier et al., 2016; Mudryk et al., 2015). Snow water equivalent (SWE) estimates require snow density to convert snow depth into mass, but snow density can be difficult to accurately approximate, due to spatial variability across snowy watersheds and temporal variability across seasons (Feng et al., 2022). While snow water equivalent is critical for direct hydrology calculations, snow depth provides the basis for estimating SWE and is subject to its own challenges. For example,

---

* Corresponding author.
E-mail address: ellynenderlin@boisestate.edu (E.M. Enderlin).

https://doi.org/10.1016/j.rse.2022.113307
Received 20 May 2022; Received in revised form 1 September 2022; Accepted 6 October 2022

snow accumulation varies over a wide range of spatial scales, such that large-scale estimates of snow depth cannot be reliably extrapolated from sparse in situ observations (Elder et al., 1991; Grünewald et al., 2010; McGrath et al., 2018; Winstral and Marks, 2014; Winstral et al., 2002). Airborne lidar has proven to be an invaluable tool to map snow depth variability at watershed scales (Deems et al., 2013; Painter et al., 2016), but it requires expensive repeat lidar flights in order to collect reference (i.e., snow-free) and snow-covered terrain elevations, and is not feasible everywhere. Similar elevation-differencing approaches applied to satellite image-derived digital elevation models (DEMs) have been recently explored, and show some promise (Deschamps-Berger et al., 2020), but the high-precision stereo pairs needed to create high resolution DEMs are irregularly acquired. Mapping snow depth using unmanned aerial vehicles empowers more flexibility with data acquisition frequency for local snow surveys with accurate georeferencing, but is limited to catchment scales (e.g. <5 km^2), and so cannot measure the global reaches that satellites survey (e.g., Bühler et al., 2016; Harder et al., 2020; Revuelto et al., 2021).

Here we test whether seasonal elevation transects acquired by the photon-counting lidar onboard the Ice, Cloud, and land Elevation, Satellite (ICESat-2), launched in September 2018, can be used to construct accurate snow depth transects at watershed and larger spatial scales. We focus on accuracy assessment of ICESat-2 level 3A data products, specifically the ATL06 Land Ice Height and ATL08 Land and Vegetation Height products, as these have been pre-processed to provide the best estimates of terrain elevations in glacierized and non-glacierized settings, respectively. We analyze ~3 years of ICESat-2 data for two study sites – Reynolds Creek Experimental Watershed (RCEW) in Idaho's Owyhee Mountains and Wolverine Glacier in southcentral Alaska's Kenai Mountains. These sites represent span a broad spectrum of climate and terrain regimes, have accurate snow-off reference elevation maps, and have been the focus of numerous prior analyses of seasonal snow accumulation (Marks et al., 2001, 2002; McNeil et al., 2019; O'Neel et al., 2019; Winstral and Marks, 2014; Winstral et al., 2002). Our analysis yields insights into the primary sources of uncertainty and bias in ICESat-2-derived snow depths and potential methodological improvements that could further increase the utility of ICESat-2 snow retrievals in vegetated and glacierized watersheds.

2. Materials and data

2.1. Study sites

ICESat-2 data were gathered at two sites representative of middle-latitude and subpolar mountain snowpack: Reynolds Creek Experimental Watershed (RCEW) in southwestern Idaho and Wolverine Glacier on the Kenai Peninsula of Alaska (Fig. 1). Each site is described in detail in the paragraphs below. These sites were selected because (1) they span an array of slopes, aspects, and vegetation types and (2) they are part of long-term government observational efforts by the USDA and USGS (Marks et al., 2001; O'Neel et al., 2019), respectively, and therefore have a wealth of supporting datasets. Specifically, both sites have high-resolution reference elevation data required for ICESat-2 snow-depth estimation and a history of detailed in situ observations focused on seasonal snow accumulation (e.g., Baker et al., 2018; Marks et al., 2001; Winstral and Marks, 2014).

Reynolds Creek Experimental Watershed (239 km^2; Fig. 1b; 43.3241 N, −116.6858E), is a north-facing watershed that drains to the Snake River (Seyfried et al., 2001). Its location in the rain shadow of the Cascade Mountains results in low precipitation rates, <250 mm/yr at the lowest elevations increasing to >1100 mm/yr at the highest elevations (~2100 m a.s.l.). The winter rain-snow transition zone typically falls above 1500 m a.s.l. (Godsey et al., 2018), with snow dominating the hydrologic budget at higher elevations. Snow survey data suggest the peak snow depth regularly exceeds 1.0 m above ~2000 m a.s.l. (Winstral and Marks, 2014), and range from ~0.2–0.9 m at the SNOTEL site at 1707 m a.s.l. (https://wcc.sc.egov.usda.gov/nwcc/site?sitenum=2029) and ~ 0.1–0.5 m at ~1500 m a.s.l. (Godsey et al., 2018). Spatial

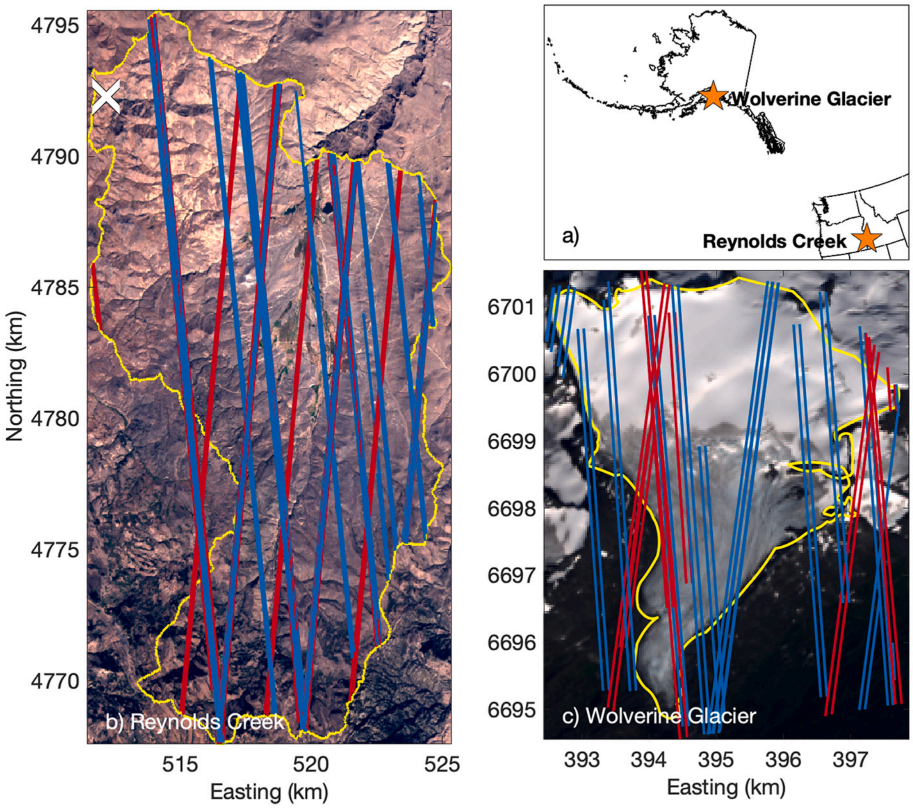

Fig. 1. A) Overview map of study sites in Idaho and Alaska. Outlines (yellow lines) for b) Reynolds Creek Experimental Watershed (RCEW) in Idaho and c) Wolverine Glacier in Alaska overlain on summer 2020 Landsat 8 true-color images. The blue and red lines in the study site maps mark the snow-on (October–June) and snow-off (July–September) ICESat-2 transects from cycles 1–13, respectively. The white X in panel b) marks the location of the RCEW SNOTEL site (site 2029; 43.2833°N, −116.85°E). c) The stark contrast in brightness between the white snow of the accumulation zone and grayer exposed ice in the ablation zone marks the end-of-melt-season snowline for Wolverine Glacier. (For interpretation of the references to color in this figure legend, the reader is referred to the web version of this article.)

variations in snow depth are largely controlled by elevation and wind redistribution (Godsey et al., 2018; Winstral and Marks, 2014). Wind redistribution is strongly controlled by aspect, with the formation of large 2+ meter drifts on north-facing slopes driven by predominantly southerly winds during winter storms, as well as vegetation (Winstral and Marks, 2014). Vegetation varies with elevation, with sagebrush steppe at the lowest elevations, transitioning upwards through mountain sagebrush, western juniper, aspen, and coniferous trees at the highest elevations (Seyfried et al., 2001).

As part of the USGS Benchmark Glacier Project, glacier mass balance, meteorology and streamflow records have been maintained since the mid 1960s at Alaska's Wolverine Glacier (Fig. 1c; 60.40°N, -148.92°E; Baker et al., 2018; McNeil et al., 2019; O'Neel et al., 2019; Zeller et al., 2022). The glacier is located in a subpolar maritime climate typical of

Table 1

ICESat-2 track dates, number of level 3A product segments, and the median and median of the absolute deviation (MAD) elevation residuals between the level 3A and reference datasets, Δz, for each snow-off (pale red) and snow-on (pale blue) season for RCEW and Wolverine Glacier.

Site	Water Year	Date	Segments	Median Δz (meters)	MAD Δz (meters)
RCEW	2018-2019 (WY19)	2018/11/26	91	-1.19	1.55
		2019/02/25	30		
		2019/08/26	962	0.12	0.57
		2019/08/28	1199		
	2019-2020 (WY20)	2019/11/25	182	0	0.67
		2020/01/26	763		
		2020/02/23	1251		
		2020/02/26	711		
		2020/05/25	830		
		2020/08/23	139	-0.16	0.69
		2020/08/26	507		
	2020-2021 (WY21)	2020/11/22	296	0.15	0.6
		2020/12/21	430		
		2021/01/23	64		
		2021/02/21	529		
		2021/02/23	1132		
		2021/05/24	39		
		2021/07/23	680	-0.13	0.68
		2021/08/21	23		
		2021/08/24	498		
		2021/09/22	1021		
Wolverine	2018-2019 (WY19)	2019/02/24	289	4.38	1.14
		2019/02/26	683		
		2019/05/27	488		
		2019/08/25	111	-0.6	1.05
		2019/08/26	625		
	2019-2020 (WY20)	2019/11/24	699	1.2	0.46
	2020-2021 (WY21)	2020/11/23	773	2.11	1.89
		2021/02/21	769		
		2021/05/21	304		
		2021/05/22	195		
		2021/06/19	40		
		2021/08/22	1029	-1.34	0.63
		2021/09/18	922		
		2021/09/20	20		

southcentral Alaska and perhumid coastal rain forests. In 2018 the total ice-covered area was ~15.6 km^2, with measured horizontal speeds up to 64 m/yr (McNeil et al., 2019). The average horizontal speed is estimated as 38 m/yr (Millan et al., 2022) and vertical speeds reach up to 6 m/yr (Zeller et al., 2022), as described in the Methods section. In recent years, the equilibrium line altitude (where snow annual accumulation is equal to melt) has been at ~1235 m above mean sea level (Zeller et al., 2022), with a glacier-wide mean annual balance rate of −0.77 m water equivalent (w.e.) per year since 1990 (O'Neel et al., 2019). In situ data from 2013 to 2017 suggest the maximum annual snow depth on the glacier is typically ~12–15 m (McGrath et al., 2018). Variations in snow depth across the glacier are strongly controlled by elevation, with a winter surface mass balance gradient of ~4.4 m w.e. per kilometer elevation gain (McGrath et al., 2018).

2.2. ICESat-2 elevation transects

The scientific instrument of ICESat-2 is a six-beam laser altimeter called the Advanced Topographic Laser Altimeter System (ATLAS). ICESat-2 is configured for a 91 day repeat interval of its reference ground tracks in the polar regions, with off-track pointing at subpolar latitudes to optimize global coverage of vegetation. Each of the six ATLAS beams utilizes a 532-nm wavelength (green) laser operating at 10,000 Hz, resulting in an along-track ground spacing of ~0.7 m, with a ground segment diameter of ~11 m (Markus et al., 2017). For the relatively flat and highly reflective terrain for which ICESat-2 is designed to map, ~10 of the ~10^{14} photons that are transmitted with each pulse are returned to the satellite and detected by the sensor (~150 photons per 11 × 11 m^2 area). The beams are separated into three pairs; the interpair distance is 3 km and the intrapair distance is 90 m. One beam in each pair is the strong beam that sends four times as many photons per laser shot as the weak beam in the pair.

The large relatively dense spatial coverage of ATLAS data, as well as the complicated interactions between the photons and varied terrain types, complicate efforts to create custom processing pipeline for geolocated photon returns (i.e., level 2A ATL03 product) for each scientific application. To facilitate data use, the photon data have been preprocessed for a number of terrain types and science applications. Level 3A data products are available for land ice height, sea ice height and freeboard, land and vegetation height, ocean surface and inland water height, and atmospheric layer characteristics. We use the level 3A, version 5 land and vegetation height (ATL08) and land ice height (ATL06) data products for October 2018 – December 2021 (Table 1) because these products are designed to provide the best estimates of terrain height in potentially-vegetated and glacierized regions, respectively. Simplified descriptions of the algorithms used to create the ATL08 and ATL06 products, along with the spatial resolution and estimated uncertainties of these products, are presented in the subsections below. We refer the reader to the ATL08 (Neuenschwander et al., 2021) and ATL06 (Smith et al., 2021) algorithm theoretical basis documents for more detailed descriptions of the level 3A products used herein.

2.2.1. ATL08: Land and vegetation height

The ATL08 product was designed to provide estimates of terrain and canopy height for every ~140 photons. In vegetated terrain, <4 return photons are expected for each photon pulse, such that the ATL08 products are provided for 100 m-long segments at 100 m intervals along each beam's track. To estimate terrain and canopy heights from geolocated photon data, the data are parsed in 10 km lengths then filtered to eliminate solar background noise. The remaining (signal) photons are detrended and a moving window is applied to classify vegetation cover based on the spread in heights. Finally, an iterative median filter is applied to identify the underlying terrain.

For each 100 m-long ATL08 segment within the Reynolds Creek Experimental Watershed, we extracted the coordinates and mean terrain and canopy height relative to the World Geodetic System 1984 (WGS84) ellipsoid (Neuenschwander et al., 2021). Estimated vertical accuracy for ATL08 products is terrain-dependent, with sub-meter uncertainties in relatively flat and sparsely-vegetated regions and 1–2 m for more complex terrain (Neuenschwander and Pitts, 2019). To facilitate the identification of snow-covered areas, we also extracted the brightness flag for each segment. The brightness flag parameter uses a radiometric approach to label a segment as "bright" if it exceeds one photon returned per pulse for the strong beam and a quarter photon per pulse for the weak beam (Neuenschwander and Pitts, 2019). For terrestrial environments, bright returns are the most likely for snowy terrain and smooth bodies of water, and we use the brightness flag here to identify and exclude non-static features from coregistration (described in section 3.1).

2.2.2. ATL06: Land ice height

The ATL06 product was designed to provide estimates of surface heights for highly-reflective terrestrial ice bodies (i.e., glaciers, ice caps, ice shelves, and ice sheets), enabling the adoption of a smaller segment length than ATL08. ATL06 products are provided for 40 m-long segments at 20 m intervals along each beam's track. As with ATL08, solar background noise photons are first filtered from the geolocated photon data. Next, the vertical and horizontal windows over which to compute photon statistics are iteratively refined based on the concentration of photon returns and confidence in their interpretation as non-noise photons. A least-squares fitting approach is then used to model the terrain heights within the window. Finally, terrain heights are corrected for biases associated with saturation of ATLAS' photon-counting detectors for highly reflective flat surfaces (i.e., first photon bias).

For each 40 m-long ATL06 segment within the 2018 GLIMS Wolverine Glacier polygon and ~ 20 km^2 of neighboring low-elevation ice-free terrain, we extracted the coordinates and mean land ice height relative to the World Geodetic System 1984 (WGS84) ellipsoid (Smith et al., 2021). Although ATL06 heights are not partitioned into terrain and canopy like ATL08 and will include vegetation where present in off-ice regions, the ATL06 data are processed to minimize the ≤0.1 m but highly variable first photon bias (Smith et al., 2021). Vertical bias and precision have been estimated as <0.03 m and < 0.09 m, respectively, for the smooth and flat Antarctic Ice Sheet interior but with a strong slope dependency (Smith et al., 2019). Because the glacier surface elevations vary over time as the result of glacier flow and the imbalance between snow accumulation and snow and ice ablation (O'Neel et al., 2019), the off-ice data are used for coregistration to the reference elevation maps (described in section 3.1).

2.3. Reference elevation maps

Due to the non-repeating nature of ICESat-2 tracks at our study sites, independent reference elevation datasets were needed to detect changes in the surface elevation related to snow accumulation and melt. High-quality (decimeter-scale uncertainties, meter-scale spatial resolution) reference elevation datasets exist for both study sites, allowing confident evaluation of ICESat-2 acquisitions with and without snow cover.

For RCEW we used an August 2014 airborne lidar-derived bare-earth digital terrain model (DTM), wherein overlying vegetation was segmented from terrain elevations. Terrain elevations were provided as a 1 m-resolution raster (Fig. 1; Ilangakoon et al., 2016). Uncertainties in terrain elevations vary with terrain parameters, as described in Ilangakoon et al. (2018), and are on the order of 10 cm. DTM elevations were provided relative to the North American Datum 1983 in the horizontal (EPSG: 26911) and the North American Vertical Datum 1988 (EPSG: 5103) geoid heights in the vertical, requiring reprojection to UTM coordinates (EPSG:32611) with respect to the WGS84 ellipsoid (EPSG: 4326) prior to differencing (gdal.io). Although spatially variable, the transformation resulted in adjustments of ~17 m in the vertical and 10s of meters in the horizontal.

To account for the changing glacier geometry, annual reference digital elevation models (DEMs) were used for Wolverine Glacier. End-of-melt season geodetic DEMs exist for each year in our study (McNeil et al., 2019; O'Neel et al., 2019). For 2018 and 2020, we used 2 m-resolution Worldview DEMs from stereo imagery acquired on 12 September 2018 and 19 October 2020, respectively. For 2019, we used a 0.5 m-resolution airborne lidar-derived DEM collected on 20 September. Although the 2020 DEM was acquired nearly one month later in the year than the other reference elevation datasets, air temperatures recorded near the glacier margin were above freezing through October 10th and the Landsat image record indicates little snow had accumulated off-ice prior to October 20th, suggesting elevation bias introduced by early season snow is likely small (McNeil et al., 2019). Uncertainties are on the order of ~3 m for Worldview DEMs (Shean et al., 2016), and 10 cm for the lidar DEM, but can be larger in vegetated off-glacier terrain and where glacier features (e.g., crevasses, melt ponds, sastruggi) evolve over time. The quoted DEM uncertainties are less than the uncertainty introduced by the temporal evolution of the glacier's surface, and the thickness of maritime snowpacks that characterize the field site. Both coregistration and elevation residuals extraction use the reference DEM with the closest acquisition date preceding the ATL06 time stamp, therefore, potential horizontal or vertical offsets between reference DEMs can be ignored. All reference data at Wolverine did not require datum transformations as they were provided in UTM coordinates with respect to the WGS84 ellipsoid (EPSG:32606).

3. Methods

Estimation of snow depths using an elevation-differencing approach requires precise coregistration between datasets, particularly in regions with highly variable terrain characteristics, so that the difference between elevation datasets (i.e., elevation residuals) can be confidently attributed to snow. In Section 3.1, we describe the coregistration process used to align the independent datasets and minimize systematic biases in their elevations. Differences between coregistered transects and reference elevations are generically referred to as Δz, or Δz^{ATL08} and Δz^{ATL06} when specifically referencing the ATL08 and ATL06 datasets, respectively. Quantification of terrain-dependent, spatially-variable biases in Δz that remain following coregistration is described in sections 3.2 and 3.3. The spatially-variable elevation biases are described in section 4, along with comparisons between in situ snow observations at RCEW and Wolverine Glacier and the bias-corrected elevation residuals, $\Delta z^{ATL08}_{adjusted}$ and $\Delta z^{ATL06}_{adjusted}$, respectively. Since we are interested in snow depths, the data are parsed into snow-off (i.e., summer; July–September) and snow-on (October–June) seasons for each hydrologic year (October–September) throughout sections 3 and 4. For the glacierized site, the hydrologic year is roughly equivalent to the mass balance year. For all figures, colors distinguish the snow-off (reds/pinks) and snow-on (blues) seasons, as in Fig. 1.

3.1. *Coregistration*

Each ICESat-2 segment was coregistered as a transect, not segment-by-segment, to eliminate systematic biases between the datasets. For coregistration and subsequent analysis, we used the mean elevation within segment footprints since this metric is provided for both ATL08 and ATL06 products and can be quickly extracted from the reference datasets.

A gradient-descent approach was applied to objectively identify and minimize three-dimensional offsets between ICESat-2 transect and reference elevation datasets. This approach inherently assumed minimization of the vertical offset between each ICESat-2 transect and the reference elevation dataset when properly coregistered. The coregistration code and the rest of the processing pipeline are available at (https://github.com/CryoGARS-Glaciology/ICESat2-snow-code.git).

Horizontal offsets were expected to be on the order of meters or less since the geolocation error for ICESat-2 is estimated as ~3.5 m (Bae et al., 2021). Therefore, we started with an initial guess of zero horizontal offset and computed the root-mean-square (RMS) elevation difference between all segments in each ICESat-2 transect and the appropriate reference elevation dataset. Each transect was iteratively shifted horizontally until the global RMS minimum was identified. The median elevation difference between all horizontally-coregistered snow-off segments and the appropriate reference elevation datasets were then used for vertical coregistration. This bulk vertical coregistration approach assumed that the ICESat-2 elevation bias relative to a reference dataset is static in time. Although a transect-specific vertical coregistration approach would be preferred if snow-covered areas were reliably eliminated from coregistration, the use of snow-off vertical biases for coregistration ensured preservation of any snow signal.

Thin snow cover is expected for RCEW, therefore, we assumed that exclusion of bright ATL08 segments was sufficient to remove bias in *horizontal* coregistration associated with snow cover. The median horizontal offsets for all non-bright segments were 0 m for both the Easting and Northing. Vertical offsets for the horizontally-coregistered segments are shown in Fig. 2. The median ± median of the absolute deviation (MAD) of the snow-off vertical offsets was −0.76 ± 0.64 m, indicating that ICESat-2 under-estimated terrain elevations relative to the RCEW reference DTM prior to vertical coregistration. The median vertical offset was subtracted from the ATL08 elevations to eliminate systematic bias in elevation residuals (i.e., median snow-off $\Delta z^{ATL08} = 0$).

The evolving surfaces of glaciers prohibit their use for coregistration. Therefore, we coregistered ATL06 transects using segments over stable off-glacier terrain. For each transect, the reference elevation map from the closest preceding acquisition date was used for coregistration. Median horizontal offsets were 0 m in both horizontal directions, with a range of 2.2 m in Easting and 2.9 m in Northing. Vertical offsets for the horizontally-coregistered segments are shown in Fig. 3. The median ± MAD of the snow-off off-glacier elevation differences was −2.51 ± 0.89 m (Fig. 3), indicating ATL06 generally under-estimated terrain elevations relative to the Wolverine reference elevation maps prior to vertical coregistration. As with the ATL08 dataset, the median vertical offset was subtracted from the ATL06 elevations to eliminate systematic bias in elevation residuals (i.e., median snow-off off-glacier $\Delta z^{ATL06} = 0$).

3.2. *Terrain parameter comparison*

Previous snow depth analyses at these study sites (McGrath et al., 2018; Winstral and Marks, 2014), and elsewhere (Clark et al., 2011; Grünewald et al., 2010; Lehning et al., 2011; Saydi and Ding, 2020; Winstral et al., 2002), indicate that terrain characteristics strongly control snow depth. Terrain parameters previously shown to strongly influence snow depth include: elevation, slope, aspect (i.e., degrees counterclockwise from south) and vegetation type and structure (e.g., Armesto and Martínez, 1978; Ivanov et al., 2008; Luus et al., 2013; Yang et al., 2020). Surface slope and vegetation can also influence the accuracy and precision of terrain elevations computed from stereoscopic imagery and lidar (e.g., Neuenschwander and Magruder, 2016; Neuenschwander et al., 2020; Shean et al., 2016; Tinkham et al., 2014). Therefore, we compared elevation residuals for coregistered segments (i.e., Δz) to the corresponding elevation, slope, and aspect. The local slope and aspect were calculated for each raster cell using the ©Matlab gradientm function applied to the appropriate reference elevation maps. For RCEW, vegetation height from a 1 m-resolution airborne lidar-derived canopy height map for 10–18 November 2007 was included as well (Shrestha and Glenn, 2016). For consistency with the Δz calculations, we use the mean terrain parameter value within each segment for our analysis.

To characterize the potential terrain-dependency of Δz, we binned snow-off and snow-on Δz according to each individual terrain parameter. The number of bins was manually selected to divide the majority of the observations fairly uniformly, with consideration for commonly-used bin widths and ease of interpretation (i.e., aspect binned into 8

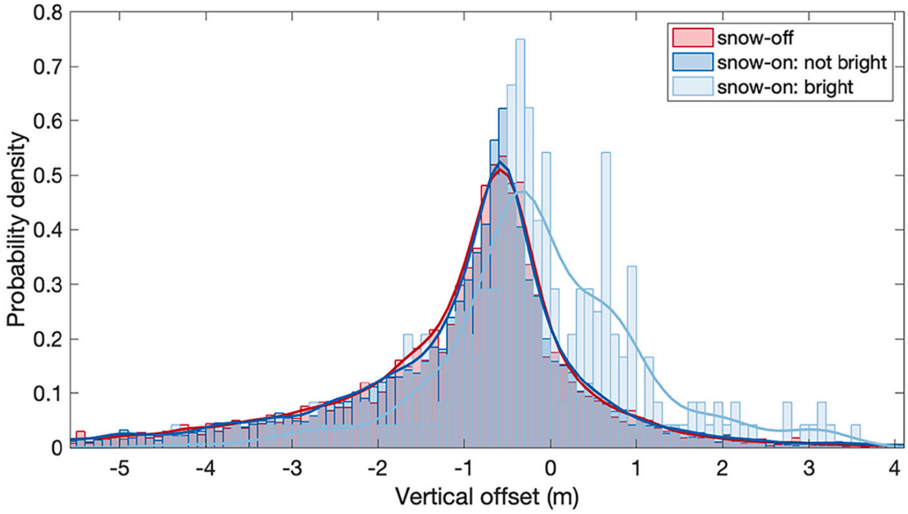

Fig. 2. Non-parametric kernel distributions of vertical co-registration offset (m) of RCEW ATL08 segments overlain on normalized probability density histograms. Warm (red/pink) colors depict vertical offsets in snow-off conditions. Cool (blue) colors depict offsets for the snow-on portion of the year, parsed by brightness flag. (For interpretation of the references to color in this figure legend, the reader is referred to the web version of this article.)

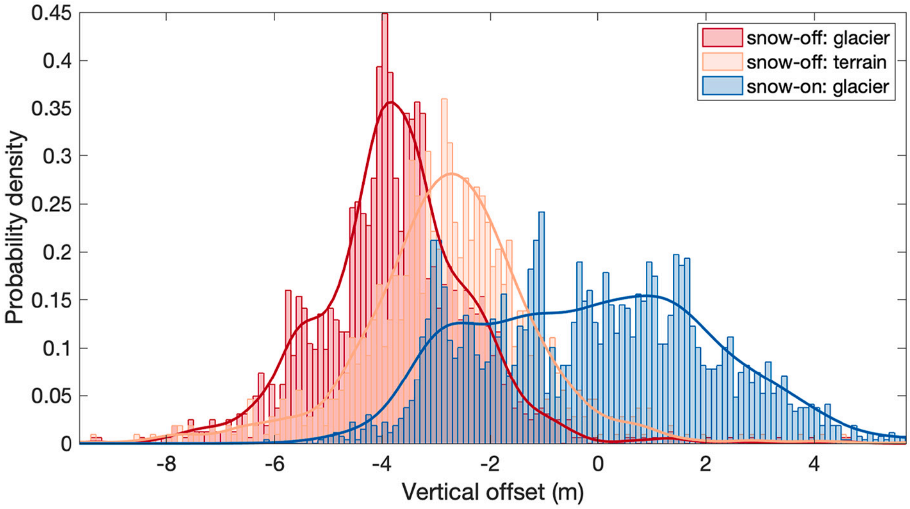

Fig. 3. Probability density function of vertical offsets (m) for Wolverine Glacier ATL06 segments. Warm (red/pink) colors depict vertical offsets in snow-off conditions, parsed for the glacier and surrounding terrain. Cool (blue) colors depict vertical offsets over the glacier surface for the snow-on portion of the year. (For interpretation of the references to color in this figure legend, the reader is referred to the web version of this article.)

tertiary intercardinal directions, elevation binned in 100 m increments). There is no appreciable influence on data interpretation for ±2 bins relative to those selected. For each terrain parameter bin, the median of Δz is used to characterize bias (i.e., systematic offset) and the MAD and interquartile range (IQR) of Δz are used to characterize uncertainty (i.e., random variability).

3.3. Snow depth estimation

Snow depth estimation requires the precise removal of any elevation biases between ICESat-2 and the reference elevation datasets. Coregistration removes uniform biases between the datasets but does not account for spatial or temporal variations in bias. A recent analysis of ATL08 data for 40 U.S. watersheds found that the accuracy and precision of ATL08 elevations vary with slope: bias increases from ~0 m to 1 m and root mean square error increases from ~0.6 m to 7.5 m for slopes from 0 to 5° to slopes >30° (Liu et al., 2021). Based on the non-linear dependence of ATL08 elevation residuals with slope in Liu et al. (2021) and observed for RCEW, we estimated the slope-dependent bias for each ATL08 segment using a quadratic function fit to the median Δz^{ATL08} binned by slope (Table 2; $R^2 = 0.996$). Slope-dependent bias-adjusted Δz^{ATL08} (i.e., $\Delta z^{ATL08}_{adjusted}$) are compared to snow depth observations in section 4.1.

Glaciers are generally more shallow-sloped than non-glacierized terrain, minimizing slope-dependent biases. However, the conversion of Δz^{ATL06} to estimates of glacier elevation change requires consideration of intra-annual changes in glacier surface elevation due to the compaction of snow remaining from previous years and vertical ice flow (submergence and emergence). Snow compaction and vertical ice flow estimates from ice-penetrating radar acquired in 2016, 2017, and 2020 from Zeller et al. (2022) were used to adjust the reference surface elevations to correct for sub-annual changes in the end-of-melt-season surface elevation assuming a constant rate of compaction- and flow-driven surface elevation change over the study period. Specifically, for each ATL06 segment, the product of the time elapsed since the reference DEM was acquired and the mean Zeller et al. (2022) submergence/

Table 2

Best-fit polynomials that model elevation residuals (Δz) as a function of elevation, slope, and aspect. Polynomials were fit to the medians of binned Δz for each terrain parameter. The coefficient of determination (i.e., R^2) for each fit is listed in parentheses after each equation. All snow-off (pale red) and snow-on (pale blue) observations are aggregated for each site. Best-fit polynomials for the bias-adjusted elevation residuals ($\Delta z_{adjusted}$) as a function of elevation are listed as the coregistered and bias-adjusted processing level.

Site	Processing Level	Season	Elevation (z; meters)	Slope (s; degrees)	Aspect (a; degrees counterclockwise from south)
RCEW	coregistered (Δz)	snow-off	$4.81 \times 10^{-4}z-0.924$ (0.45)	$-4.24 \times 10^{-3}s^2+0.040s+0.073$ (0.996)	$-0.312\cos(a-52.9)-0.07$ (0.900)
		snow-on	$1.48 \times 10^{-3}z-2.49$ (0.821)	$-4.53 \times 10^{-3}s^2+0.056s+0.029$ (0.976)	$-0.286\cos(a-44.3)-0.04$ (0.684)
	coregistered + bias-adjusted ($\Delta z_{adjusted}$)	snow-off	$-5.48 \times 10^{-5}z+0.156$ (0.009)		
		snow-on	$1.03 \times 10^{-3}z-1.52$ (0.844)		
Wolverine	coregistered (Δz)	snow-off	$4.65 \times 10^{-3}z-7.07$ (0.971)	$-3.77 \times 10^{-4}s^2+0.023s-1.43$ (0.256)	$0.422\cos(a+85.6)-1.24$ (0.764)
		snow-on	$3.63 \times 10^{-3}z-1.35$ (0.945)	$-0.010s^2+0.032s+1.59$ (0.986)	$0.745\cos(a+85.8)+2.95$ (0.970)
	coregistered + bias-adjusted ($\Delta z_{adjusted}$)	snow-off	$1.47 \times 10^{-2}z-19.3$ (0.913)		
		snow-on	$1.02 \times 10^{-2}z-9.25$ (0.592)		

emergence velocity for grid cells overlapping the segment was subtracted from the corresponding reference elevation. The surface evolution-adjusted Δz^{ATL06} (i.e., $\Delta z^{ATL06}_{adjusted}$) are compared to winter and annual surface mass balance observations in section 4.2.

4. Results

For each study site, we summarize key characteristics of Δz and $\Delta z_{adjusted}$ with respect to terrain parameters. Since snow accumulation and melt can vary tremendously between years, the data are parsed into hydrologic/mass balance years, hereafter referred to as water years for

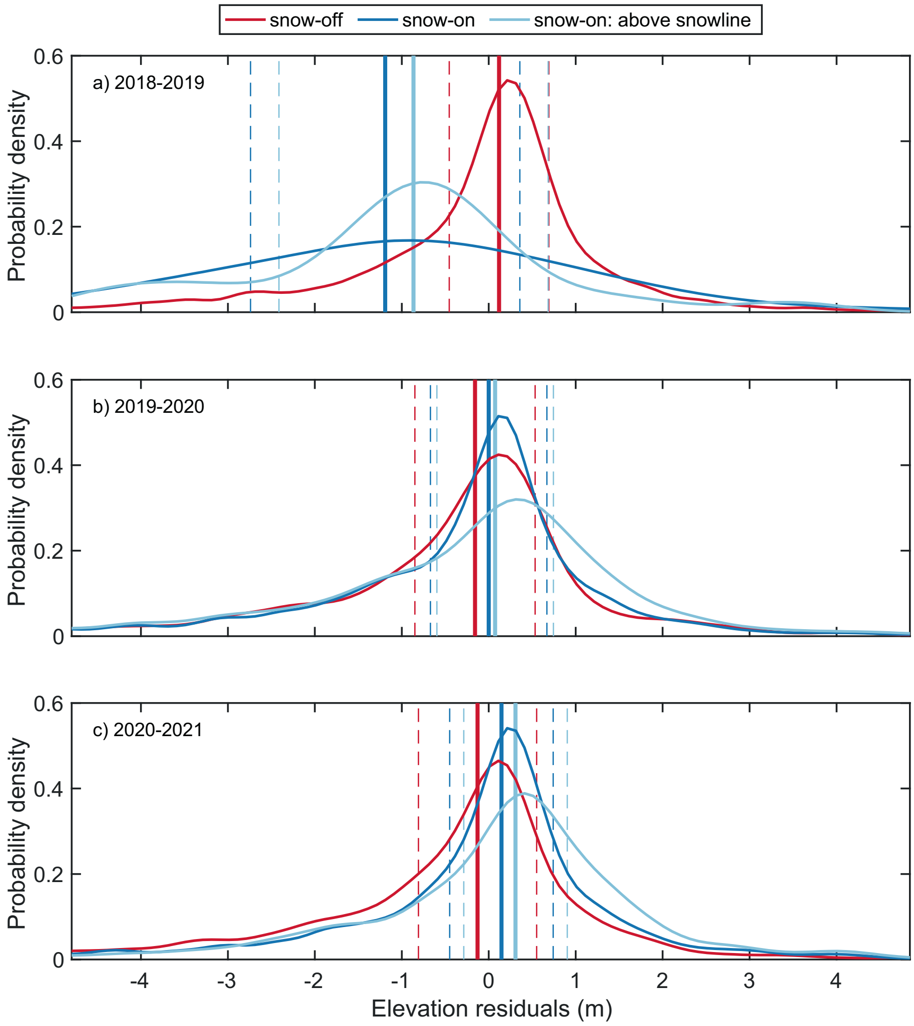

Fig. 4. Non-parametric kernel distributions for RCEW Δz^{ATL08} for a) WY19, b) WY20, and c) WY21 (1 Oct – 30 Sept). The data are parsed into snow-off (red; July–September) and potentially snow-on (blues; October–June) portions of the year. Since the rain-snow transition line is within the watershed, the distributions for all snow-on segments (blue) and snow-on segments only above the seasonal snowline (light blue) are plotted to facilitate identification of the snow signal. The solid vertical line marks the median and the dashed vertical lines bracket the median ± the median of the absolute deviation (MAD) for each distribution. The same seasonal color scheme is used in Fig. 2. $\Delta z^{ATL08} < 0$ indicate an under-estimation of elevations by the ICESat-2 ATL08 dataset following coregistration. (For interpretation of the references to color in this figure legend, the reader is referred to the web version of this article.)

simplicity: 2018–2019 = WY19, 2019–2020 = WY20, and 2020–2021 = WY21.

4.1. RCEW: ATL08 case study in vegetated terrain

The seasonal Δz^{ATL08} distributions are left-skewed, with a longer tail for negative residuals during all observation periods (Fig. 4). The median Δz^{ATL08} for all snow-off segments is 0 m because the snow-off segments were used for vertical coregistration (Fig. 2). The MAD Δz^{ATL08} for all snow-off segments is 0.64 m (Fig. 4). There are only two observation dates with a total of 121 snow-on segments for RCEW during WY19. Only 69 snow-on segments were recorded above the

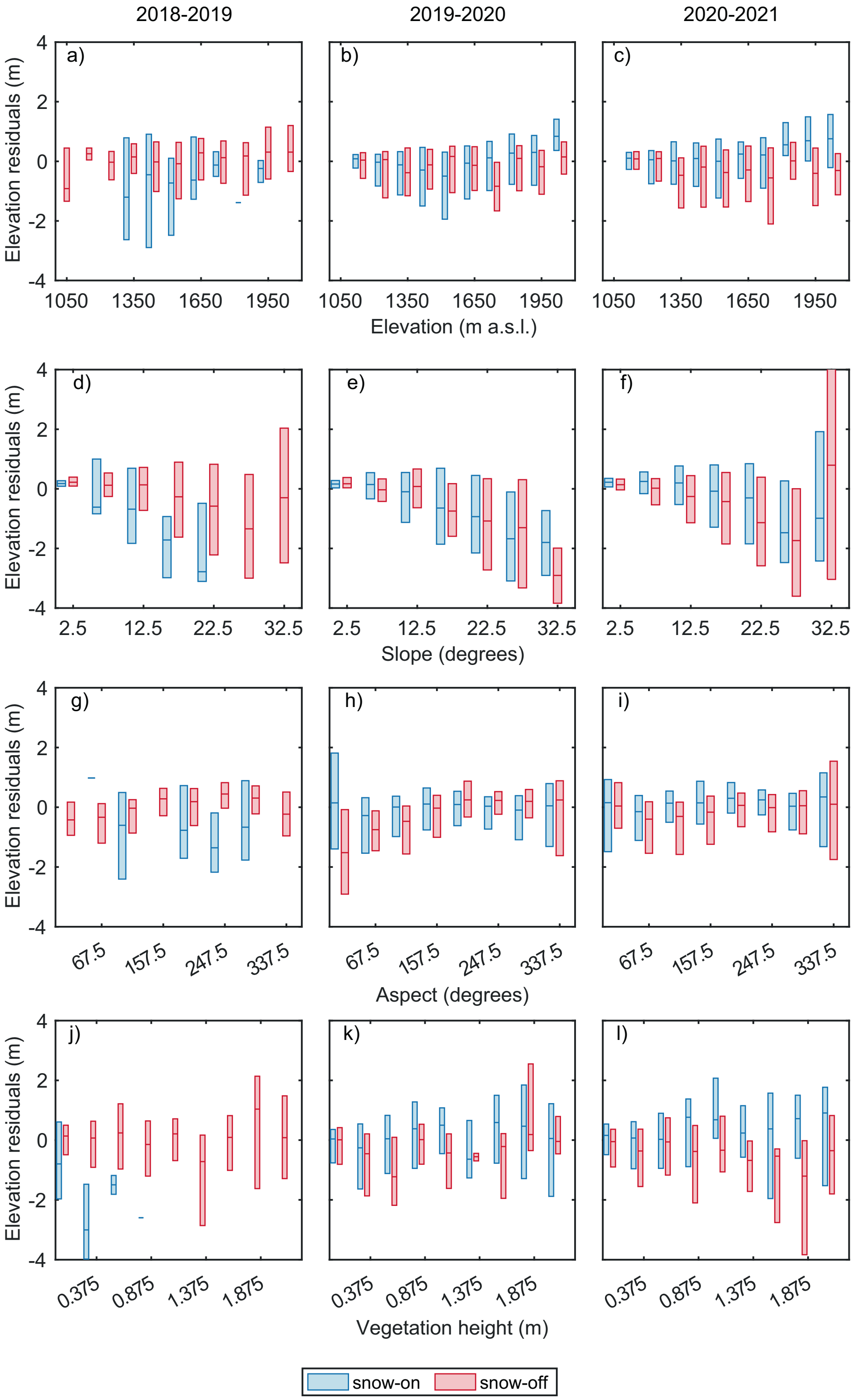

Fig. 5. Box plots of Δz^{ATL08} plotted against a-c) elevation, d-f) slope, g-i) aspect, and j-l) vegetation height for RCEW. Colors distinguish seasons (see legend). Data are parsed into water year (columns). Boxes bound the 25th to 75th percentiles and horizontal lines mark the medians of the binned elevation residuals. Full seasonal box plots, including outliers, for the entire study period are shown in Fig. S1.

typical snowline and they span a narrow range of terrain characteristics, potentially biasing the WY19 Δz^{ATL08} characteristics in Figs. 4 and 6. Therefore, WY19 snow-on data are excluded from further analysis. For WY20 and WY21, the Δz^{ATL08} distributions are qualitatively similar for the snow-off and snow-on periods, but *P*-values from two-sample Kolmogorov-Smirnov tests indicate that the snow-on distributions are significantly different from the snow-off distributions at the 95% confidence level.

The boxplots in Fig. 5 demonstrate Δz^{ATL08} terrain dependency. The boxplots show the IQR (vertical box extent) and median (horizontal line within each box) for Δz^{ATL08} relative to each terrain parameter. Whiskers extending to the full range of nonoutlier values as well as markers for outliers (i.e., values $>3 \times IQR$ from the IQR) are included in the boxplots in Fig. S1. RCEW snow-off Δz^{ATL08} are independent of elevation, but vary non-linearly with both slope and aspect (Fig. 5). There is a pronounced increase in bias and uncertainty in Δz^{ATL08} with increasing slope up to $\sim 30^\circ$. As slope increases from $\sim 0^\circ$ to $\sim 30^\circ$, bias becomes progressively more negative (median Δz^{ATL08}=[0.19, −2.07] m) and the spread of the residuals increases (MAD Δz^{ATL08}=[0.17, 2.13] m, IQR Δz^{ATL08}= [0.34, 4.30] m); this indicates that estimating snow depth from ATL08 elevations in steep mountain terrain is likely to be highly uncertain. The decrease in the medians of the slope-binned Δz^{ATL08} is best described with a quadratic function (Table 2). There are too few data for slopes $>30^\circ$ to quantify slope effects (Fig. S2). A slight sinusoidal variation in snow-off Δz^{ATL08} with aspect is also evident (Table 2). Much of RCEW is sparsely vegetated, such that the vast majority of segments have a mean vegetation height $<$ 1 m (Fig. S2) and there is no apparent relationship between snow-off Δz^{ATL08} and vegetation height (Fig. 5). Unlike the snow-off data, snow-on Δz^{ATL08} from 2019 to 2021 increase with elevation above the snowline (Table 2). The relationships between snow-on Δz^{ATL08} and slope, aspect, and vegetation height are comparable to the relationship evident in the snow-off data (Fig. 5; Table 2).

The probability density functions for the snow-off and snow-on Δz^{ATL08} and slope dependency-adjusted Δz^{ATL08} (i.e., $\Delta z^{ATL08}_{adjusted}$) are shown in Fig. 6a and the slope-dependent adjustment is shown in Fig. 6b. The slope adjustment reduces the negative skew of the elevation residuals (Fig. 6a), but does not improve their precision: the snow-off MAD Δz^{ATL08} = 0.64 m and snow-off MAD $\Delta z^{ATL08}_{adjusted}$ = 0.63 m, with unchanged slope-dependency for both the MAD and IQR. The slope-dependent adjustment reduces the apparent dependency of the snow-off $\Delta z^{ATL08}_{adjusted}$ with elevation and strengthens the relationship between snow-on $\Delta z^{ATL08}_{adjusted}$ and elevation with respect to the relationships observed for Δz^{ATL08} (Table 2).

Given the large uncertainty in $\Delta z^{ATL08}_{adjusted}$, we compare the seasonal timing of brightness-flagged returns and inter-annual variations in $\Delta z^{ATL08}_{adjusted}$ to the snow depth time series at the RCEW SNOTEL site to assess whether ATL08 can be used to reliably map snow cover. Over the past two decades, snow has typically been recorded at the SNOTEL site (1707 m a.s.l.) from mid-November through March. Eleven of twenty-one ATL08 transects were acquired during the typical snow-on season but only four transects contained brightness-flagged segments: 23/02/2020, 26/02/2020, 21/02/2021, and 23/02/2021. The majority (80%) of the flagged segments were located at elevations above the common rain-snow transition line (Fig. 7, ~1500 m a.s.l.; Godsey et al., 2018),

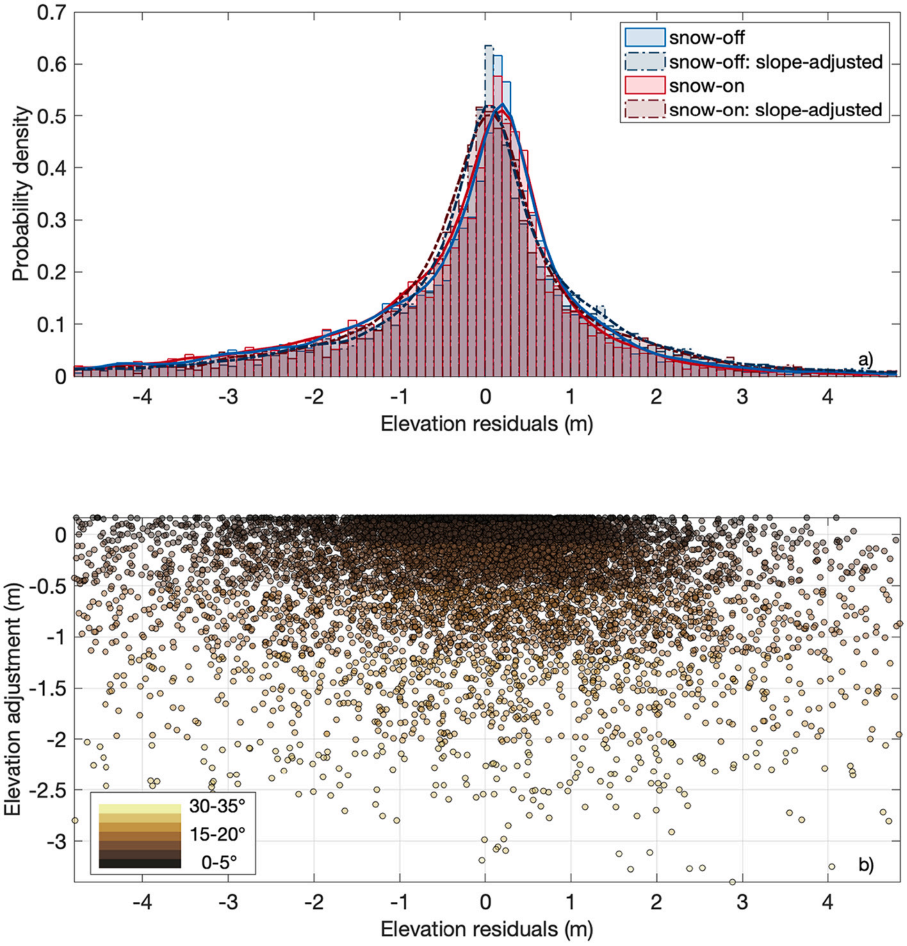

Fig. 6. The effects of slope-dependent elevation adjustments for RCEW. a) Snow-off (reds) and snow-on (blues) non-parametric distribution curves for Δz^{ATL08} and $\Delta z^{ATL08}_{adjusted}$. Line hue and style distinguish whether the slope-dependent adjustment has been applied, with lighter solid lines for Δz^{ATL08} and darker dashed lines for $\Delta z^{ATL08}_{adjusted}$. b) Scatterplot of $\Delta z^{ATL08}_{adjusted}$ plotted against the slope-dependent adjustment. The scatterplot symbol color varies with slope (see inset color bar).

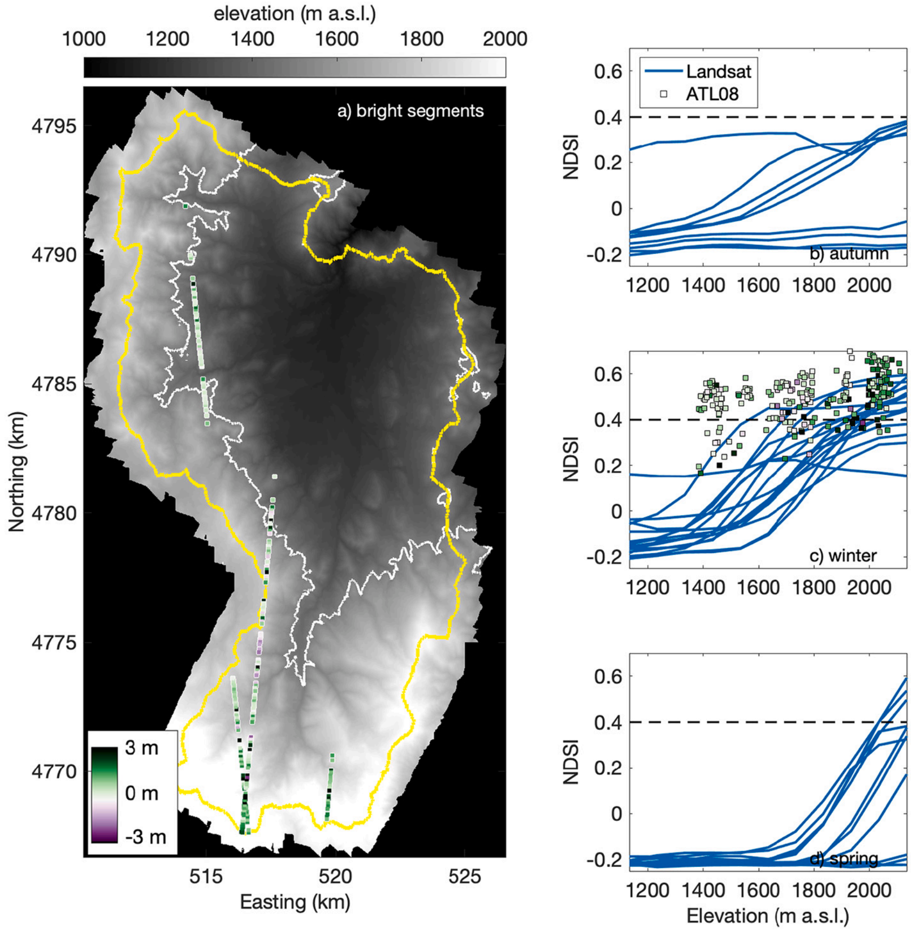

Fig. 7. Elevation distribution of likely snow-covered regions in the RCEW. a) Map of $\Delta z_{adjusted}^{ATL08}$ for exceptionally bright segments (colored squares; see color bar). The background image is the reference elevation map for the watershed (grayscale color bar). The watershed extent is outlined in yellow and the typical snowline is delineated in white. b-d) Seasonal elevation-averaged profiles of the Normalized Difference Snow Index (NDSI) from 2018 to 2021 Landsat 8 images acquired during the typical snow-on season (blue lines). The dashed black line denotes the common threshold used to identify snow (NDSI>0.4). The brightness-flagged segments are plotted according to elevation and average NDSI from the two Landsat 8 images with the closest acquisition dates. (For interpretation of the references to color in this figure legend, the reader is referred to the web version of this article.)

consistent with seasonal snow cover, but <10% of each transect was flagged as bright. Elevation profiles of the normalized difference snow index (NDSI) calculated using Landsat imagery corroborate that snow was under-reported by the brightness flag: application of the common NDSI range of 0.4–1.0 for snow (Vermote et al., 2016) to the snow-on Landsat images for RCEW suggests that high-elevation snow is common from January–April over the ICESat-2 era (Fig. 7). Therefore, analyses of $\Delta z_{adjusted}^{ATL08}$ should not be restricted to segments that are identified as exceptionally bright.

Above the seasonal snowline, large-scale spatial and temporal patterns in snow-on $\Delta z_{adjusted}^{ATL08}$ are in good agreement with in situ snow observations. The majority (~67%) of the snow-on segments for WY20 and WY21 are nearly coincident in time with peak snow depths at the RCEW SNOTEL site (February 18th in WY20 and February 20th in WY21), facilitating intercomparison of the datasets. For WY20, the median $\Delta z_{adjusted}^{ATL08}$ above the snowline is 0.06 m and the SNOTEL peak snow depth is 0.44 m. For WY21, the median $\Delta z_{adjusted}^{ATL08}$ above the snowline is 0.31 m and the SNOTEL peak snow depth is 0.69 m. Even though the median $\Delta z_{adjusted}^{ATL08}$ is negatively biased with respect to the SNOTEL peak snow depth during WY20 and WY21, the bias is consistent (0.38 m) over time, suggesting that inter-annual variations in $\Delta z_{adjusted}^{ATL08}$ reflect temporal variations in seasonal snowpack. Additionally, we find that snow-on $\Delta z_{adjusted}^{ATL08}$ increase by ~1 m per kilometer above the seasonal snowline (Table 2), consistent with the measured precipitation gradient for the watershed (Nayak et al., 2010).

4.2. Wolverine glacier: ATL06 case study in glacierized terrain

The snow-off, off-glacier data below the seasonal snowline (1235 m a.s.l.) are used to vertically coregister the Wolverine data and subsequently assess temporal variations in glacier Δz^{ATL06}. Hereafter we refer to these data as "off-glacier" for simplicity. The off-glacier MAD $\Delta z^{ATL06} = 0.89$ m (Fig. 8). There is no apparent relationship between the off-glacier Δz^{ATL06} and elevation or slope (Fig. 9). *P*-values from two-sample Kolmogorov-Smirnov tests indicate that all seasonal distributions of glacier Δz^{ATL06} are significantly different from the off-glacier Δz^{ATL06} distributions at the 95% confidence level.

Snow-off glacier Δz^{ATL06} represent the sum of snow accumulation, snow, firn, and ice melt, snow and firn compaction, and vertical ice flow since the beginning of the water year. The spatial variations in each of these processes are complex, and a detailed description of their variations at Wolverine Glacier is beyond the scope of our analysis, but general patterns are summarized below to facilitate interpretation of glacier Δz^{ATL06}. In the accumulation zone, where snow persists year-round, snow accumulation causes glacier thickening (increasing Δz^{ATL06}) that is countered by surface submergence (i.e., downwards motion) due to firn compaction and ice flow (decreasing Δz^{ATL06}). In the ablation zone, winter snow accumulation and year-round mass transport from the accumulation zone and surface emergence (i.e., upwards motion) due to vertical flow cause thickening (increasing Δz^{ATL06}) that is countered by melt (decreasing Δz^{ATL06}).

For Wolverine Glacier, the majority of the snow-off glacier Δz^{ATL06} are negative (Fig. 8; Table 1), indicating widespread lowering of the glacier surface consistent with independent observations of negative glacier-wide mass balance of −1.87 m w.e., −1.46 m w.e., and − 1.81 m w.e. in 2018, 2019, and 2020 respectively (McNeil et al., 2019). However, the snow-off glacier Δz^{ATL06} are not normally distributed, reflecting differences in mass balance processes between the high-elevation accumulation zone and low-elevation ablation zone (Fig. 1.; white and gray glacier regions, respectively). When paired with the terrain

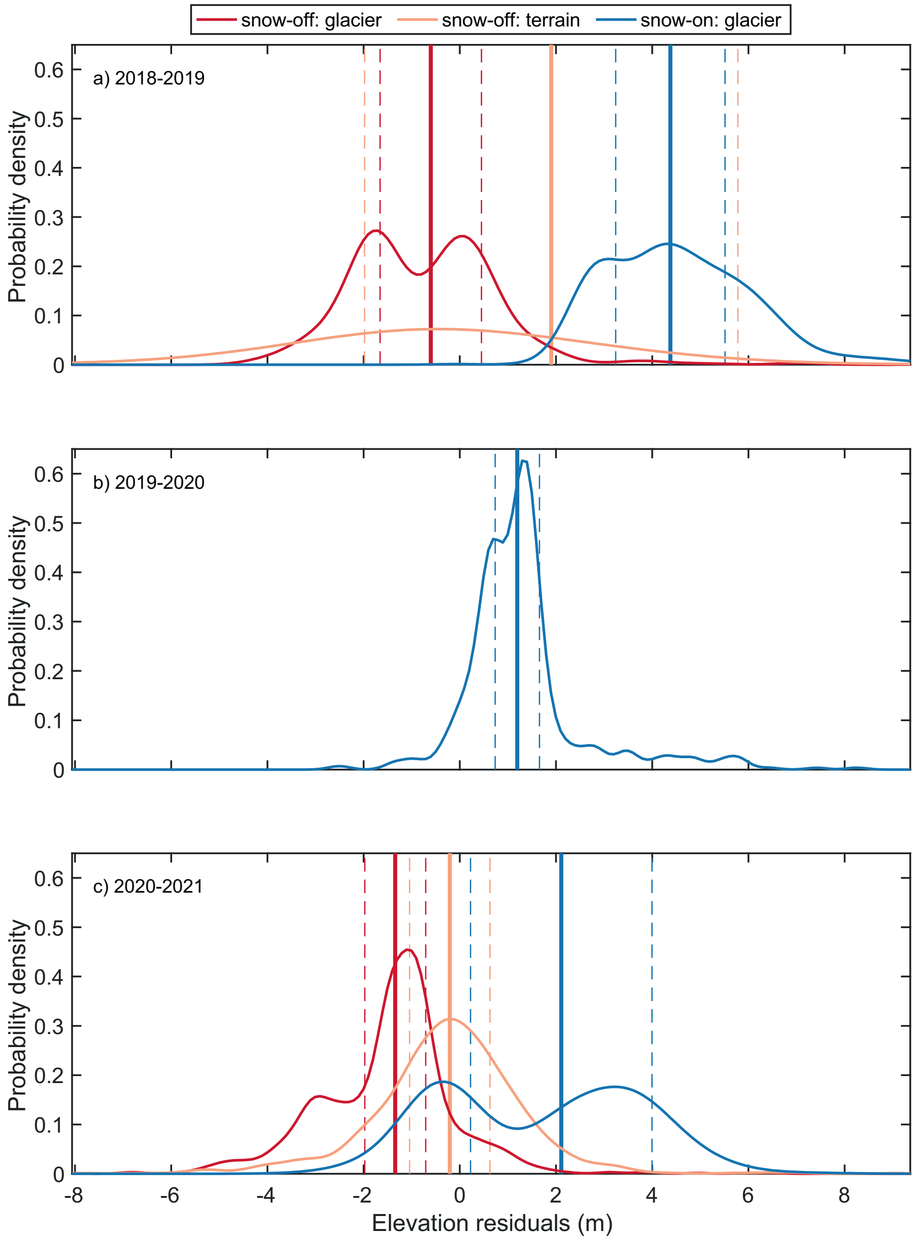

Fig. 8. Non-parametric kernel distributions for Wolverine Glacier Δz^{ATL06} for a) WY19, b) WY20, and c) WY21. The data are parsed into snow-off (red/pink; July–September) and potentially snow-on (blues; October–June) portions of the year. Since the snow-off off-glacier segments were used for coregistration, the snow-off segments are parsed according to location: glacier (red) and surrounding terrain (pink). The solid vertical line indicates the median and the dashed vertical lines bracket the median ± the median of the absolute deviation (MAD) for each distribution. The same seasonal color scheme is used in the vertical error distributions in Fig. 3. $\Delta z^{ATL06} < 0$ indicate an underestimation of elevations by the ICESat-2 ATL06 dataset following coregistration. (For interpretation of the references to color in this figure legend, the reader is referred to the web version of this article.)

parameters, we find that the snow-off glacier Δz^{ATL06} are strongly positively linearly correlated with elevation (Fig. 9; Table 2) but do not consistently vary with either slope or aspect (Fig. 9; Table 2). As with the snow-off glacier data, the snow-on Δz^{ATL06} are positively linearly correlated with elevation but have no consistent relationship with either slope or aspect (Fig. 9; Table 2). Full seasonal boxplots, including outliers, are shown in Fig. S3 and histograms of the glacier terrain parameters are shown in Fig. S4.

Adjustment of the reference glacier surface elevations to account for emergence/submergence of the glacier surface relative to the beginning of the water year isolates the surface mass balance (i.e., difference between snow accumulation and snow, firn, and ice ablation) component of the glacier's total mass balance. The intra-annual adjustment of the glacier surface markedly alters the shape of the $\Delta z^{ATL06}_{adjusted}$ distributions (Fig. 10a; dashed lines) relative to the Δz^{ATL06} distributions (Fig. 10a; solid lines), indicating that the surface mass balance cannot be estimated directly from Δz^{ATL06}. The magnitude of the reference elevation adjustment is the product of the emergence/submergence velocity and the time separation between the ICESat-2 and reference elevation acquisitions. Therefore, the adjustment is generally larger for the snow-off portion of the year because they have the longest time separation relative to the preceding end-of-melt-season reference elevation map (Fig. 10b; symbol size).

After accounting for emergence/submergence of the glacier surface, we find that snow-off $\Delta z^{ATL06}_{adjusted}$ strongly increase with elevation (Table 2). Surface melt dominates accumulation below the seasonal snowline, with net ablation of 4.0 m in WY19 and 5.1 m in WY21 at 950 m a.s.l.. Accumulation dominates melt in the upper reaches of the glacier, with annual net accumulation of 6.0 m in WY19 and 3.7 m in WY21 at 1650 m a.s.l.. To convert $\Delta z^{ATL06}_{adjusted}$ to estimates of annual surface mass balance in water equivalent, $\Delta z^{ATL06}_{adjusted}$ is multiplied by the ratio of the density of the snow, firn, or ice at the glacier surface to the density of water (1000 kg/m^3). We use a density of 440 kg/m^3 from McGrath et al. (2018) above the snowline and 850 kg/m^3 from Huss (2013) below the seasonal snowline. Following O'Neel et al. (2019), we estimate the average annual mass balance gradient using piecewise linear fits with

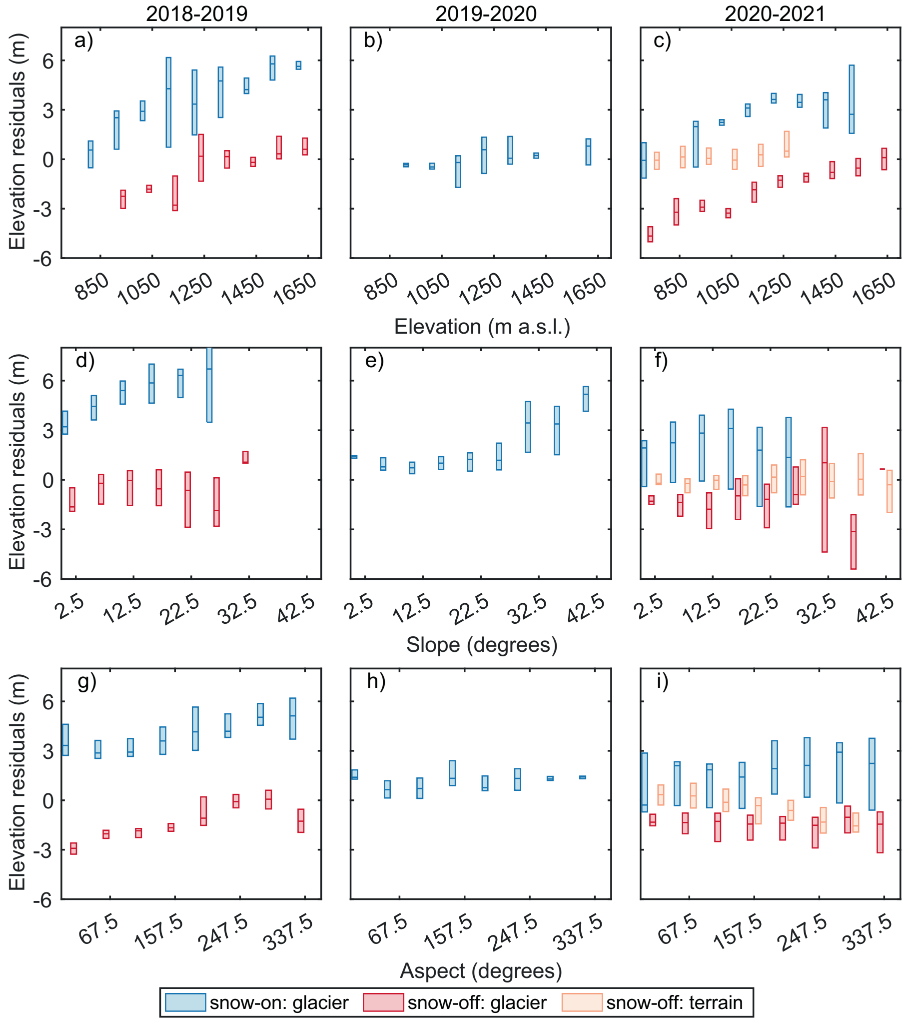

Fig. 9. Box plots of Δz^{ATL06} plotted against a-c) elevation, d-f) slope, and g-i) aspect for Wolverine Glacier. Colors distinguish seasons (see legend). Data are parsed into water year (columns). Boxes bound the 25th to 75th percentiles and horizontal lines mark the medians of binned Δz^{ATL06}. Full seasonal box plots, including outliers, for the entire study period are shown in Fig. S3.

the breakpoint at the snowline (O'Neel et al., 2019). The average annual surface mass balance gradient above the snowline is ~5.1 m w.e./km and below the snowline is ~15.5 m w.e./km. In comparison, the annual mass balance gradient calculated from in situ observations collected during the 1966–2018 period was ~8 m w.e./km (O'Neel et al., 2019) and the winter surface mass balance gradient from repeat ice-penetrating radar surveys varied between 3.48 and 6.24 m w.e./km during the 2013–2017 period (McGrath et al., 2018).

5. Discussion

Satellite-based lidar systems provide invaluable observations of temporal changes in volume of the polar ice sheets and sea ice and airborne lidar provides valuable observations of spatial variations in snow depth and volume. However, prior to this study, the feasibility of mountain snow mapping using satellite-based lidar has not been fully assessed. Accurate satellite lidar-derived snow depth transects could be valuable for the development of terrain parameters used for spatial extrapolation of sparse in situ observations (e.g., Deems et al., 2008; Trujillo et al., 2009; Winstral and Marks, 2014) and/or validation of snow models (e.g., Winstral and Marks, 2002).

Below we discuss the feasibility of ICESat-2 level 3A data products for quantification of mountain snow depth along transects using two end-member study sites: vegetated, semi-arid Reynolds Creek Experimental Watershed (RCEW) in Idaho, and maritime Wolverine Glacier in Alaska. At the most basic level, snow depths can be estimated as the difference between snow surface (i.e., snow-on) and snow-free terrain (i.e., snow-off) elevations. However, reliable estimates of snow depth from this elevation differencing approach depend on the accuracy and precision of both the ICESat-2 terrain elevations and the snow-off reference elevation datasets. For independent terrain elevations, as required for non-repeating ICESat-2 transects, biases between the datasets must be corrected. Below we discuss difficulties associated with the conversion of elevation residuals to snow depths based on the results for our study sites and provide recommendations for future methodological improvements for ICESat-2 snow depth mapping.

5.1. Snow depth estimates from elevation residuals

5.1.1. Non-glacierized terrain

For the vegetated semi-arid RCEW in southwestern Idaho, we find that ICESat-2 ATL08 data can be used to estimate watershed-scale variations in snow depth over time, with uncertainties in snow depth of ~0.6 m. In line with Liu et al. (2021), we find non-linear slope-dependent errors in ATL08 terrain heights, ranging from 0.19 ± 0.34 m for slopes 0–5° to 2.07 ± 4.30 m for slopes from 25 to 30° for RCEW. While the slope-dependent *bias* can be minimized, such that watershed-scale variations in snow depth can be inferred from $\Delta z^{ATL08}_{adjusted}$ (Table 2), the

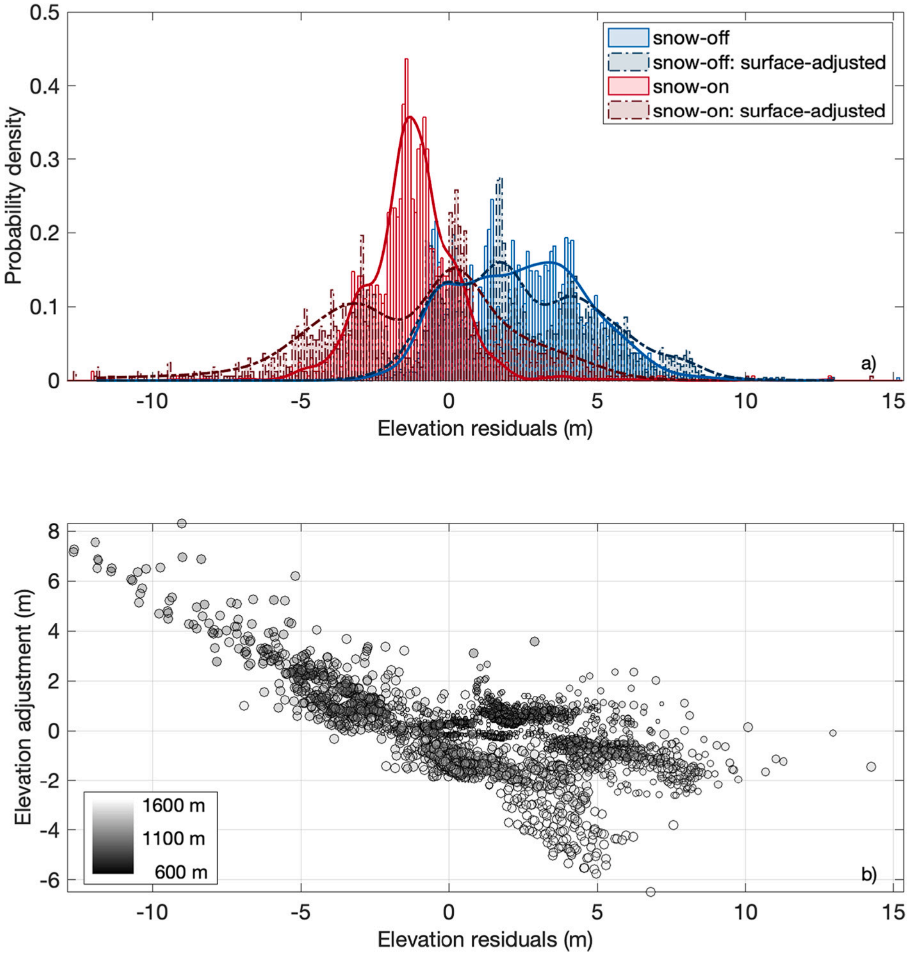

Fig. 10. The effects of submergence/emergence-based reference elevation adjustments for Wolverine Glacier. a) Snow-off (reds) and snow-on (blues) non-parametric distribution curves for Δz^{ATL06} and $\Delta z^{ATL06}_{adjusted}$. Line hue and style distinguish whether the surface evolution adjustment has been applied, with lighter solid lines for Δz^{ATL06} and darker dashed lines for $\Delta z^{ATL06}_{adjusted}$. b) Scatterplot of $\Delta z^{ATL06}_{adjusted}$ plotted against the surface elevation adjustment. The scatterplot symbol color varies with elevation (see inset color bar). The scatterplot symbol size varies with time separation between the reference elevation map and ATL06 acquisitions.

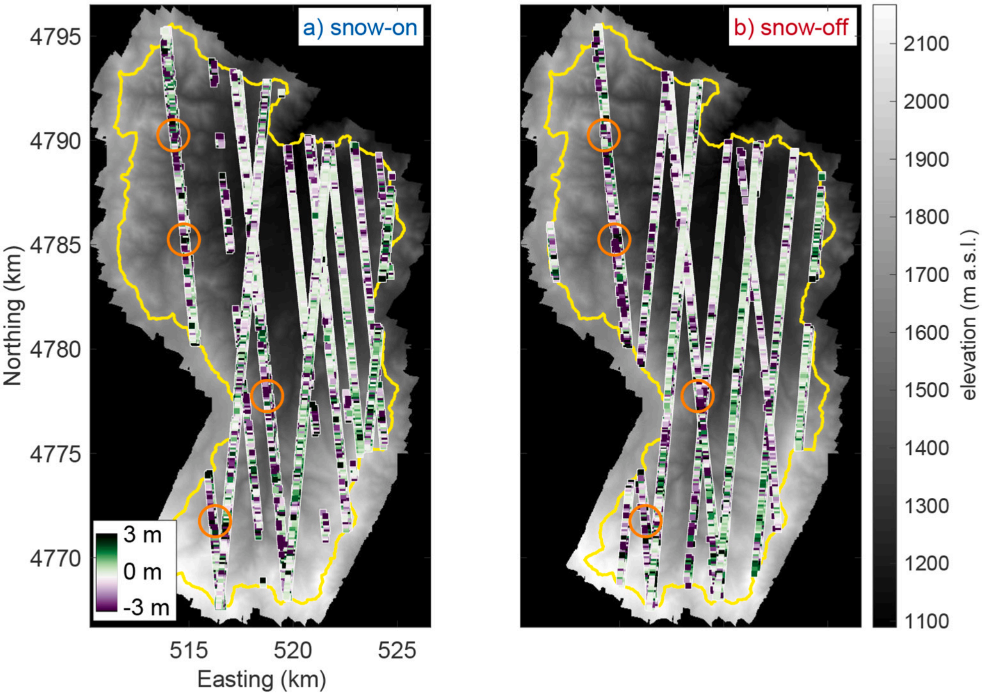

Fig. 11. Maps of a) snow-on and b) snow-off $\Delta z^{ATL08}_{adjusted}$ for RCEW. The magnitude of the $\Delta z^{ATL08}_{adjusted}$ is indicated by symbol color. Greens indicate $\Delta z^{ATL08}_{adjusted} > 0$ (i.e., ATL08 elevations greater than reference elevations) and purples indicate $\Delta z^{ATL08}_{adjusted} < 0$ (i.e., ATL08 elevations less than reference elevations). Orange circles highlight several regions with persistently negative $\Delta z^{ATL08}_{adjusted}$. The background image is the reference elevation map for the watershed (grayscale color bar). The watershed extent is outlined in yellow. (For interpretation of the references to color in this figure legend, the reader is referred to the web version of this article.)

increase in uncertainty with slope will be problematic in many mountain regions, where slopes are often $>25^\circ$ and uncertainties will obscure the snow signal (Figs. 5-6).

Application of a slope-dependent adjustment reduces the negative skew of $\Delta z_{adjusted}^{ATL08}$ relative to Δz^{ATL08} (Fig. 6), yet large uncertainties in $\Delta z_{adjusted}^{ATL08}$ remain. Particularly problematic are the stationary meters-scale negative elevation residuals evident in both the snow-on and snow-off datasets (Fig. 11, orange circles). The year-round persistence of the negative elevation residuals suggests that they are caused by differences in vegetation removal from the ATL08 and reference terrain elevations. The accuracy of ATL08 terrain elevations has been found to vary with percent vegetation cover (Neuenschwander et al., 2020) and inadequate removal of vegetation from airborne lidar observations is known to dramatically increase uncertainties in terrain elevations (e.g., Klápště et al., 2020; Reutebuch et al., 2003; Spaete et al., 2010; Su and Bork, 2006). In RCEW, vegetation type and structure are strongly dependent on the aspect of the terrain (Mitchell et al., 2015; Shrestha and Glenn, 2016). Therefore, although we do not find any clear relationships between Δz^{ATL08} and mean vegetation height, spatial variations in vegetation cover may explain the observed aspect-dependency of Δz^{ATL08} (Fig. 5g-i, Table 2). Thus, even where high-quality reference elevations are available, varying vegetation effects on the accuracy of ATL08 and reference terrain elevations prevents estimation of snow depths at the segment scale. The increase in uncertainty with slope and vegetation observed for RCEW is in line with the sub-meter uncertainties in relatively flat and sparsely-vegetated regions and 1–2 m for more complex terrain quoted for ATL08 (Neuenschwander and Pitts, 2019). Thus, ATL08 data are best suited for the estimation of watershed-scale patterns in snow depth (e.g., snow depth variations with elevation) in unglacierized mountain regions with relatively low-slopes and sparse vegetation cover.

5.1.2. Glacierized terrain

For Wolverine Glacier in southcentral Alaska, we find that ATL06 surface mass balance gradients are in good agreement with independent estimates (McGrath et al., 2018; O'Neel et al., 2019). While the difference between off-glacier snow-off ATL06 terrain heights and reference surface elevations suggest that uncertainties in ATL06-derived surface mass balance are ~0.8 m, the intercomparison of the elevation datasets is likely influenced by the presence of vegetation in the ATL06 terrain heights. For low-slope regions, ATL06 uncertainties are estimates as <0.1 m (Smith et al., 2021). We do not observe a slope-dependency for off-glacier snow-free Δz^{ATL06} (Fig. 9), but our observations are limited in space and time.

For glacierized study sites, failure to account for intra-annual variations in the end-of-melt-season glacier surface can bias the interpretation of Δz^{ATL06} (Fig. 10). For Wolverine Glacier, we use independent estimates of surface emergence/submergence and firn compaction to adjust the reference elevation datasets to account for intra-annual surface elevation change so that $\Delta z_{adjusted}^{ATL06}$ reflect the temporal evolution of the glacier due to surface mass balance processes. Failure to account for firn compaction and vertical ice flow can results in up to meters of bias in surface mass balance profiles, as demonstrated for Wolverine Glacier. Temporal variations in ICESat-2 transects can also bias the interpretation of surface mass balance profiles, as demonstrated in the plots of elevation-binned Δz^{ATL06} in Fig. 9a-c. Differences in temporal sampling with respect to the surface mass balance extrema are also evident in the surface mass balance transects in Fig. 12, with less positive surface mass balance transects corresponding to earlier acquisition dates in the snow-on season. Peak snow conditions at Wolverine are expected between mid April and the end of May, with the closest ICESat-2 observations from ~21–26 February and ~ 22–28 May, and the end of the melt season is expected in late September (O'Neel et al., 2019). Thus, even our steepest winter surface mass balance gradients may not accurately capture the snow accumulation gradient over the glacier's surface.

The timing offset between ICESat-2 acquisitions and annual surface mass balance extrema is not unique to Wolverine Glacier, or glacierized study sites in general, and will be problematic for all studies that aim to estimate maximum seasonal snow depths given that the timing of peak snowpack varies inter-annually. However, the temporal evolution of the glacier surface presents a unique challenge that complicates the application of ICESat-2 ATL06 data to mountain glaciers. If reference elevation maps do not accurately capture inter-annual variations in the end-of-melt-season surface, and/or if the snow compaction and vertical ice flow for the glacier are unknown, snow depth and surface mass balance gradients may be considerably under-estimated by ATL06.

5.2. Potential methodological improvements for snow depth estimation

Based on the observed elevation-dependency of snow depths and the ICESat-2 level 3A residuals in our two test watersheds, we conclude that ATL08 and ATL06 elevation residuals can be used to map elevation gradients in snow accumulation and melt where high-quality reference elevation maps are available, as long as vertical biases can be constrained. Snow depth accuracy and precision depends on a number of factors, including the availability of high-quality reference elevation

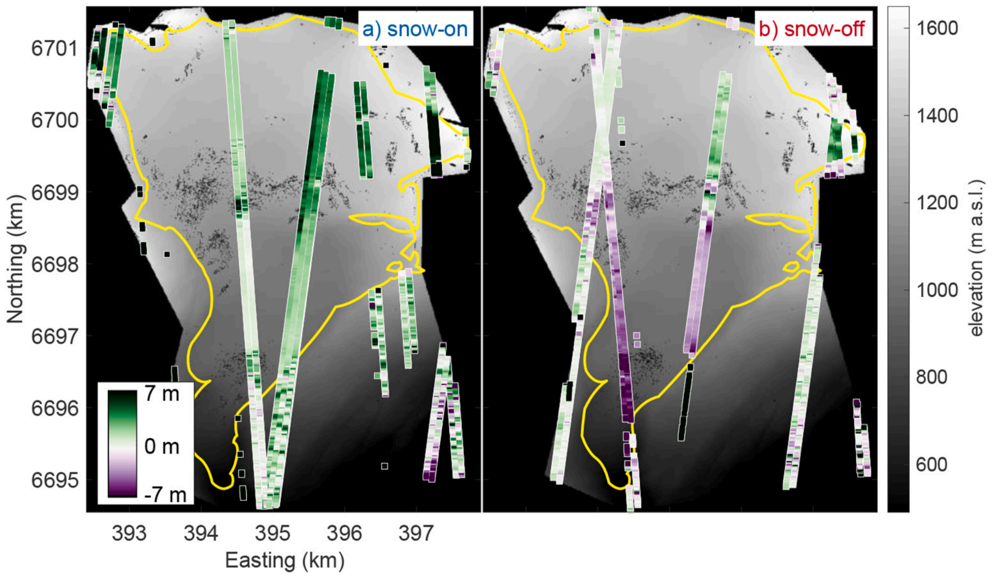

Fig. 12. Maps of a) winter surface mass balance and b) annual surface mass balance from snow-on and snow-off $\Delta z_{adjusted}^{ATL06}$, respectively, for Wolverine Glacier. The surface mass balance magnitude is indicated by symbol color, with greens indicating mass gain and purples indicating mass loss. The background image is the time-averaged reference elevation map for the watershed (see grayscale color bar). The glacier extent is outlined in yellow. (For interpretation of the references to color in this figure legend, the reader is referred to the web version of this article.)

datasets, accurate coregistration, minimization of vegetation effects, and knowledge of terrain-dependency (particularly slope) of ATL08 and ATL06 products and snow depths.

Here, we used high-quality reference elevation datasets and still found uncertainties on the order of 10s of centimeters at the transect scale, with biases of up to meters at the segment-scale. Thus, elevation residuals calculated with respect to lower-quality (i.e., less precision or lower spatial resolution) reference data would be too imprecise to estimate snow depths. More refined snow depth estimates may be possible if uncertainties can be reduced through (1) use of other ICESat-2 terrain elevation metrics, (2) cross-track weighting of reference elevations, and/or (3) custom processing of ATL03 geolocated photon clouds.

In this study compared the mean terrain height within each ICESat-2 segment to the mean over the corresponding area in the reference elevation map. The best-fit ICESat-2 terrain heights could also be used as long as the equivalent elevation metric can be extracted from the reference elevation map. Uncertainties in elevation residuals may also be reduced if the reference elevation metrics are weighted to account for the approximately gaussian cross-track distribution of ICESat-2 photons. Finally, given the relatively large number of photon returns per shot over bright snow-covered surfaces and the short spatial scales over which both terrain and snow depths vary in mountain regions, it may be beneficial to estimate terrain heights from ATL06 products custom-produced from ATL03 data in mountain regions. Custom ICESat-2 segments are currently being pursued by the NASA-supported SlideRule framework, but additional research must be executed to determine the best methods to compare ICESat-2 and reference elevation datasets.

6. Conclusions

Seasonal snow melt dominates the hydrologic budget across a large portion of the globe (Barnett et al., 2005; Beniston, 2003; Freeman et al., 2018; Huss et al., 2017; Huss and Hock, 2018; Steinbauer et al., 2018; Viviroli et al., 2007; Wrzesien et al., 2018). In situ snow observations provide valuable information regarding the temporal evolution of snow depth and density but are too sparse in to capture important spatial variability in snow depths. Airborne lidar can be used to construct spatially extensive snow depth maps, but is often limited to a single snapshot.

In this study we explore the use of ICESat-2 elevation transects as a means to map spatial variations in snow depth at the watershed scale throughout the accumulation and melt seasons. For two mountain study sites that represent end-member climate regions, we find that seasonal elevation transects from the ICESat-2 level3A ATL08 (Land and vegetation height) and ATL06 (Land ice height) data products can be used to estimate along-track gradients in snow depth in mountain watersheds where high-quality reference elevation datasets exist. We estimate that uncertainties for ATL08 terrain elevations are tens of centimeters at the watershed-scale, can exceed 1 m for individual segments, and are dependent on slope. After accounting for the non-linear slope-dependent bias, the difference in terrain elevations between ATL08 and a reference DTM captures the expected gradient in snow depths with elevation as well as temporal changes in peak snow depth. However, our analysis of ATL08 products for RCEW suggests that even where high-quality snow-off lidar-derived DTMs can be used as a reference, the increase in uncertainty with slope and spatially-isolated, systematic biases in elevation caused by inadequate terrain mapping through vegetation prevent the use of ATL08 data for segment-scale snow depth estimates in non-glacierized watersheds.

Glacierized environments pose unique challenges to the application of ICESat-2 data for snow accumulation and snow, firn, and ice melt mapping. Although glaciers generally have shallow surface slopes and are devoid of vegetation, accurate estimation of mass balance from an elevation-differencing approach requires knowledge of the temporal evolution of the glacier surface at intra- and inter-annual time scales. We make use of annual end-of-melt-season high-resolution glacier surface elevation maps generated by the USGS Benchmark Glacier program, adjusted to account for intra-annual surface evolution using independent estimates of vertical surface motion (Zeller et al., 2022), to demonstrate that ATL06 data can be used to create time series of surface mass balance gradients for mountain glaciers. While reference elevations can come from high-resolution stereo satellite image-derived DEMs in lieu of airborne lidar, enabling widespread comparison with ATL06 elevations, application to Wolverine Glacier suggests that failure to account for intra- or inter-annual evolution of the glacier surface can result in up to meters of bias in surface mass balance estimates and skew surface mass balance gradients.

Based on the case studies presented here, we conclude that ATL08 and ATL06 observations are best suited for characterization of watershed-scale snow depth/surface mass balance gradients in low-slope regions with thick snowpacks. As airborne lidar surveys become more common and additional high-resolution stereo satellite imaging platforms are deployed, the availability of the required reference datasets should expand, enabling the construction of snow depth and surface mass balance gradients throughout the accumulation and ablation seasons. These time series will be beneficial to analyses of controls on snow depth variability and validation of snow models.

Author contributions

EME conceived the project, supervised student research, updated code, analyzed data, generated figures, and wrote the manuscript. CME developed the initial coregistration and data analysis codes. MG organized codes and updated datasets. CM provided high-resolution digital elevation models and photogrammetry expertise. LS contributed submergence/emergence expertise. HPM, SO, CM, CF, and LS revised the manuscript and provided insights into controls on snow depths at the study sites.

Funding

This work was supported by the NASA EPSCoR Program [80NSSC19M0043, 80NSSC20M0222].

Declaration of Competing Interest

The authors declare that they have no known competing financial interests or personal relationships that could have appeared to influence the work reported in this paper.

Data availability

The link to code is included in the manuscript and the data can be downloaded from the NSIDC ICESat-2 data portal.

Acknowledgements

Thank you to the USGS Benchmark Glacier Program, who facilitated access to a variety of Wolverine Glacier datasets and to Dan McGrath and Lucas Zeller for sharing their emergence/submergence data for the glacier prior to publication. Any use of trade, firm, or product names is for descriptive purposes only and does not imply endorsement by the U. S. Government.

Appendix A. Supplementary data

Supplementary data to this article can be found online at https://doi.org/10.1016/j.rse.2022.113307.

References

Armesto, J.J., Martínez, J.A., 1978. Relations between vegetation structure and slope aspect in the Mediterranean region of Chile. J. Ecol. 66, 881–899.

Bae, S., Helgeson, B., James, M., Magruder, L., Sipps, J., Luthcke, S., Thomas, T., 2021. Performance of ICESat-2 precision pointing determination. Earth Space Sci. 8 (e2020EA001478) https://doi.org/10.1029/2020EA001478.

Baker, E.H., McNeil, C.J., Sass, L.C., O'Neel, S., 2018. Point Raw Glaciological Data: Ablation Stake, Snow Pit, and Probed Snow Depth Data on USGS Benchmark Glaciers, 1981-2016 (ver. 2.0, March 2022). U.S. Geological Survey data release. https://doi.org/10.5066/F76Q1WHK.

Barnett, T.P., Adam, J.C., Lettenmaier, D.P., 2005. Potential impacts of a warming climate on water availability in snow-dominated regions. Nature 438, 303–309. https://doi.org/10.1038/nature04141.

Beniston, M., 2003. Climatic change in mountain regions: a review of possible impacts. Clim. Chang. 59, 5–31. https://doi.org/10.1023/A:1024458411589.

Bühler, Y., Adams, M.S., Bösch, R., Stoffel, A., 2016. Mapping snow depth in alpine terrain with unmanned aerial systems (UASs): potential and limitations. Cryosphere 10, 1075–1088. https://doi.org/10.5194/tc-10-1075-2016.

Clark, M.P., Hendrikx, J., Slater, A.G., Kavetski, D., Anderson, B., Cullen, N.J., Kerr, T., Hreinsson, E.Ö., Woods, R.A., 2011. Representing spatial variability of snow water equivalent in hydrologic and land-surface models: a review. Water Resources Res. 47 (7) https://doi.org/10.1029/2011WR010745.

Deems, J.S., Fassnacht, S.R., Elder, K.J., 2008. Interannual consistency in fractal snow depth patterns at two Colorado mountain sites. J. Hydrometeorol. 9 (5), 977–988.

Deems, J.S., Painter, T.H., Finnegan, D.C., 2013. Lidar measurement of snow depth: a review. J. Glaciol. 59 (215), 467–479. https://doi.org/10.3189/2013JoG12J154.

Deschamps-Berger, C., Gascoin, S., Berthier, E., Deems, J., Gutmann, E., Dehecq, A., Shean, D., Dumont, M., 2020. Snow depth mapping from stereo satellite imagery in mountainous terrain: evaluation using airborne laser-scanning data. Cryosphere 14, 2925–2940. https://doi.org/10.5194/tc-14-2925-2020.

Dozier, J., Bair, E.H., Davis, R.E., 2016. Estimating the spatial distribution of snow water equivalent in the world's mountains. WIREs Water 3, 461–474. https://doi.org/10.1002/wat2.1140.

Elder, K., Dozier, J., Michaelsen, J., 1991. Snow accumulation and distribution in an alpine watershed. Water Resour. Res. 27 (7), 1541–1552. https://doi.org/10.1029/91WR00506.

Elias, E., James, D., Heimel, S., Steele, C., Steltzer, H., Dott, C., 2021. Implications of observed changes in high mountain snow water storage, snowmelt timing and melt window. J. Hydrol. Regional Studies 35. https://doi.org/10.1016/j.ejrh.2021.100799.

Feng, T., Zhu, S., Huang, F., Hao, J., Mind'je, R., Zhang, J., Li, L., 2022. Spatial variability of snow density and its estimation in different periods of snow season in the middle Tianshan Mountains, China. Hydrol. Processes 36 (8), e14644. https://doi.org/10.1002/hyp.14644.

Freeman, B.G., Lee-Yaw, J.A., Sunday, J.M., Hargreaves, A.L., 2018. Expanding, shifting and shrinking: the impact of global warming on species' elevational distributions. Glob. Ecol. Biogeogr. 27, 1268–1276. https://doi.org/10.1111/geb.12774.

Godsey, S.E., Marks, D., Kormos, P.R., Seyfried, M.S., Enslin, C.L., Winstral, A.H., McNamara, J.P., Link, T.E., 2018. Eleven years of mountain weather, snow, soil moisture and streamflow data from the rain–snow transition zone – the Johnston draw catchment, Reynolds Creek experimental watershed and critical zone observatory, USA. Earth Syst. Sci. Data 10, 1207–1216. https://doi.org/10.5194/essd-10-1207-2018.

Grünewald, T., Schirmer, M., Mott, R., Lehning, M., 2010. Spatial and temporal variability of snow depth and ablation rates in a small mountain catchment. Cryosphere 4 (2), 215–225. https://doi.org/10.5194/tc-4-215-2010.

Harder, P., Pomeroy, J.W., Helgason, W.D., 2020. Improving sub-canopy snow depth mapping with unmanned aerial vehicles: lidar versus structure-from-motion techniques. Cryosphere 14, 1919–1935. https://doi.org/10.5194/tc-14-1919-2020.

Huss, M., 2013. Density assumptions for converting geodetic glacier volume change to mass change. Cryosphere 7, 877–887. https://doi.org/10.5194/tc-7-877-2013.

Huss, M., Bookhagen, B., Huggel, C., Jacobsen, D., Bradley, R., Clague, J., Vuille, M., Buytaert, W., Cayan, D., Greenwood, G., Mark, B., Milner, A., Weingartner, R., Winder, M., 2017. Toward mountains without permanent snow and ice. Earth's Future 5, 418–435. https://doi.org/10.1002/2016EF000514.

Huss, M., Hock, R., 2018. Global-scale hydrological response to future glacier mass loss. Nat. Clim. Change 8, 135–140. https://doi.org/10.1038/s41558-017-0049-x.

Ilangakoon, N., Glenn, N.F., Spaete, L.P., Dashti, H., Li, A., 2016. 2014 Lidar-Derived 1m Digital Elevation Model Data Set for Reynolds Creek Experimental Watershed, Southwestern Idaho [Data set. https://doi.org/10.18122/B26C7X.

Ilangakoon, N.T., Glenn, N.F., Dashti, H., Painter, T.H., Mikesell, D., Spaete, L.P., Mitchell, J.J., Shannon, K., 2018. Constraining plant functional types in a semi-arid ecosystem with waveform lidar. Remote Sens. Environ. 209, 497–509. https://doi.org/10.1016/j.rse.2018.02.070.

Ivanov, V.Y., Bras, R.L., Vivoni, E.R., 2008. Vegetation-hydrology dynamics in complex terrain of semiarid areas: 1. A mechanistic approach to modeling dynamic feedbacks. Water Resources Res. 44, (3). https://doi.org/10.1029/2006WR005588.

Klápště, P., Fogl, M., Barták, V., Gdulová, K., Urban, R., Moudry, V., 2020. Sensitivity analysis of parameters and constraining performance of ground filtering algorithms with UAV photogrammetry-based and LiDAR point clouds. Internat. J. Digital Earth 13 (12), 1672–1694. https://doi.org/10.1080/1753°8947.2020.1791267.

Lehning, M., Grünewald, T., Schirmer, M., 2011. Mountain snow distribution governed by an altitudinal gradient and terrain roughness. Geophys. Res. Lett. 38 (L19504) https://doi.org/10.1029/2011GL048927.

Liu, A., Cheng, X., Chen, Z., 2021. Performance evaluation of GEDI and ICESat-2 laser altimeter data for terrain and canopy height retrievals. Remote Sens. Environ. 264 (112571) https://doi.org/10.1016/j.rse.2021.112571.

Luus, K.A., Gel, Y., Lin, J.C., Kelly, R.E.J., Duguay, C.R., 2013. Pan-Arctic linkages between snow accumulation and growing-season air temperature, soil moisture and vegetation. Biogeosciences 10, 7575–7597. https://doi.org/10.5194/bg-10-7575-2013.

Markus, T., Neumann, T., Martino, A., Abdalati, W., Brunt, K., Csatho, B., Farrell, S., Fricker, H., Gardner, A., Harding, D., Jasinski, M., Kwok, R., Magruder, L., Lubin, D., Luthcke, S., Morison, J., Nelson, R., Neuenschwander, A., Palm, S., Popescu, S., Shum, C.K., Schutz, B.E., Smith, B., Yang, Y., Zwally, J., 2017. The ice, cloud, and land elevation Satellite-2 (ICESat-2): science requirements, concept, and implementation. Remote Sens. Environ. 190, 260–273. https://doi.org/10.1016/j.rse.2016.12.029.

Marks, D., Cooley, K.R., Robertson, D.C., Winstral, A., 2001. Long- term snow database, Reynolds Creek experimental watershed, Idaho, USA. Water Resour. Res. 37 (11), 2835–2838.

Marks, D., Winstral, A., Seyfried, M., 2002. Simulation of terrain and forest shelter effects on patterns of snow deposition, snowmelt and runoff over a semi-arid mountain catchment. Hydrol. Process. 16, 3605–3626.

McGrath, D., Sass, L., O'Neel, S., McNeil, C., Candela, S.G., Baker, E.H., Marshall, H.-P., 2018. Interannual snow accumulation variability on glaciers derived from repeat, spatially extensive ground-penetrating radar surveys. Cryosphere 12, 3617–3633. https://doi.org/10.5194/tc-12-3617-2018.

McNeil, C.J., Florentine, C.E., Bright, V.A.L., Fahey, M.J., McCann, E., Larsen, C.F., Thoms, E.E., Shean, D.E., McKeon, L.A., March, R.S., Keller, W., Whorton, E.N., O'Neel, S., Baker, E.H., Sass, L.C., Bollen, K.E., 2019. Geodetic data for USGS benchmark glaciers: orthophotos, digital elevation models, glacier boundaries and surveyed positions (ver 3.0, August 2022). U.S. Geological Survey data release. https://doi.org/10.5066/P9R8BP3K.

Millan, R., Mouginot, J., Rabatel, A., Morlighem, M., 2022. Ice velocity and thickness of the world's glaciers. Nat. Geosci. 15, 124–129. https://doi.org/10.1038/s41561-021-00885-z.

Mitchell, J.J., Shrectha, R., Spaete, L.P., Glenn, N.F., 2015. Combining airborne hyperspectral and LiDAR data across local sites for upscaling shrubland structural information: lessons for HypsIRI. Remote Sens. Environ. 167, 98–110. https://doi.org/10.1016/j.rse.2015.04.015.

Mudryk, L.R., Derksen, C., Kushner, P.J., Brown, R., 2015. Characterization of northern hemisphere snow water equivalent datasets, 1981–2010. J. Clim. 28 (20), 8037–8051. https://doi.org/10.1175/JCLI-D-15-0229.1.

Nayak, A., Marks, D., Chandler, D.G., Seyfried, M., 2010. Long-term snow, climate, and streamflow trends at the Reynolds Creek experimental watershed, Owyhee Mountains, Idaho, United States. Water Resourses Res. 46 (W06519) https://doi.org/10.1029/2008WR007525.

Neuenschwander, A.L., Magruder, L.A., 2016. The potential impact of vertical sampling uncertainty on ICESat-2/ATLAS terrain and canopy height retrievals for multiple ecosystems. Remote Sens. 8 (12), 1039. https://doi.org/10.3390/rs8121039.

Neuenschwander, A., Pitts, K., 2019. The ATL08 land and vegetation height product for the ICESat-2 Mission. Remote Sens. Environ. 221, 247–259. https://doi.org/10.1016/j.rse.2018.11.005.

Neuenschwander, A., Guenther, E., White, J.C., Duncanson, L., Montesano, P., 2020. Validation of ICESat-2 terrain and canopy heights in boreal forests. Remote Sens. Environ. 251 https://doi.org/10.1016/j.rse.2020.112110.

Neuenschwander, A.L., Pitts, K.L., Jelley, B.P., Robbins, J., Klotz, B., Popescu, S.C., Nelson, R.F., Harding, D., Pederson, D., Sheridan, R., 2021. ATLAS/ICESat-2 L3A land and vegetation height, version 5. NASA National Snow and Ice Data Center Distributed Active Archive Center, Boulder, Colorado USA. https://doi.org/10.5067/ATLAS/ATL08.005. [23/02/2022].

O'Neel, S., McNeil, C., Sass, L.C., Florentine, C., Baker, E.H., Peitzsch, E., McGrath, D., Fountain, A.G., Fagre, D., 2019. Reanalysis of the US geological survey benchmark glaciers: long-term insight into climate forcing of glacier mass balance. J. Glaciol. 65, 850–866. https://doi.org/10.1017/jog.2019.66.

Painter, T.H., Berisford, D.F., Boardman, J.W., Bormann, K.J., Deems, J.S., Gehrke, F., Hedrick, A., Joyce, M., Laidlaw, R., Marks, D., Mattmann, C., McGurk, B., Ramirez, P., Richardson, M., Skiles, S.M.K., Seidel, F.C., Winstral, A., 2016. The airborne snow observatory: fusion of scanning lidar, imaging spectrometer, and physically-based modeling for mapping snow water equivalent and snow albedo. Remote Sens. Environ. 184, 139–152. https://doi.org/10.1016/j.rse.2016.06.018.

Reutebuch, S.E., McGaughey, R.J., Andersen, H.E., Carson, W.W., 2003. Accuracy of a high-resolution LiDAR terrain model under a sonifer forest canopy. Canad. J. Remote Sens. 29, 527–535.

Revuelto, J., López-Moreno, J.I., Alonso-González, E.A., 2021. Light and shadow in mapping alpine snowpack with unmanned aerial vehicles in the absence of ground control points. Water Resources Res. 57 https://doi.org/10.1029/2020WR028980 e2020WR028980.

Saydi, M., Ding, J.-L., 2020. Impacts of topographic factors on regional snow cover characteristics. Water Sci. Eng. 13 (3), 171–180. https://doi.org/10.1016/j.wse.2020.09.002.

Seyfried, M., Harris, R., Marks, D., Jacob, B., 2001. Geographic database, Reynolds Creek experimental watershed, Idaho,United States. Water Resources Res. 37 (11), 2825–2829.

Shean, D.E., Alexandrov, O., Moratto, Z.M., Smith, B.E., Joughin, I.R., Porter, C., Morin, P., 2016. An automated, open-source pipeline for mass production of digital elevation models (DEMs) from very-high-resolution commercial stereo satellite imagery. ISPRS J. Photogram. Remote Sens. 116, 101–117. https://doi.org/10.1016/j.isprsjprs.2016.03.012.

Shrestha, R., Glenn, N.F., 2016. 2007 Lidar-Derived Digital Elevation Model, Canopy Height Model and Vegetation Cover Model Data Sets for Reynolds Creek Experimental Watershed, Southwestern Idaho [Data. https://doi.org/10.18122/B27C77.

Smith, B.E., Fricker, H.A., Holschuh, N., Gardner, A., Adusumilli, S., Brunt, K.M., Csatho, B., Harbeck, K., Huth, A., Neumann, T., Nilsson, J., Siegfried, M., 2019. Land ice height-retrieval algorithm for NASA's ICESat-2 photon counting laser altimeter. Remote Sens. Environ. 233 https://doi.org/10.1016/j.rse.2019.111352.

Smith, B., Adusumilli, S., Csathó, B.M., Felikson, D., Fricker, H.A., Gardner, A., Holschuh, N., Lee, J., Nilsson, J., Paolo, F.S., Siegfried, M.R., Sutterley, T., 2021. ATLAS/ICESat-2 L3A Land Ice Height, Version 5. Boulder, Colorado USA. NASA National Snow and Ice Data Center Distributed Active Archive Center. https://doi.org/10.5067/ATLAS/ATL06.005 [23/02/2022].

Spaete, L.P., Glenn, N.F., Derryberry, D.R., Sankey, T.T., Mitchell, J.J., Hardegree, S.P., 2010. Vegetation and slope effects on accuracy of a LiDAR-derived DEM in the sagebrush steppe. Remote Sens. Lett. 2 (4), 317–326. https://doi.org/10.1080/01431161.2020.515267.

Steinbauer, M.J., Grytnes, J.A., Jurasinski, G., Kulonen, A., Lenoir, J., Pauli, H., Rixen, C., Winkler, M., Bardy-Durchhalter, M., Barni, E., Bjorkman, A.D., Breiner, F. T., Burg, S., Czortek, P., Dawes, M.A., Delimat, A., Dullinger, S., Erschbamer, B., Felde, V.A., Fernández-Arberas, O., Fossheim, K.F., Gómez-García, D., Georges, D., Grindrud, E.T., Haider, S., Haugum, S.V., Henriksen, H., Herreros, M.J., Jaroszewicz, B., Jaroszynska, F., Kanka, R., Kapfer, J., Klanderud, K., Kühn, I., Lamprecht, A., Matteodo, M., Morra di Cella, U., Normand, S., Odland, A., Olsen, S. L., Palacio, S., Petey, M., Piscová, V., Sedlakova, B., Steinbauer, K., Stöckli, V., Svenning, J.-C., Teppa, G., Theurillat, P.-P., Vittoz, P., Woodin, S.J., Zimmermann, N.E., Wipf, S., 2018. Accelerated increase in plant species richness on mountain summits is linked to warming. Nature 556, 231–234. https://doi.org/10.1038/s41586-018-0005-6.

Su, J.G., Bork, E.W., 2006. Influence of vegetation, slope and LiDAR sampling angle on DEM accuracy. Photogram. Eng. Remote Sens. 72, 1265–1274.

Tinkham, W.T., Smith, A.M.S., Marshall, H.-P., Link, T.E., Falkowski, M.J., Winstral, A. H., 2014. Quantifying spatial distribution of snow depth errors from LiDAR using random forest. Remote Sens. Environ. 141, 105–115. https://doi.org/10.1016/j.rse.2013.10.021.

Trujillo, E., Ramírez, J.A., Elder, K.J., 2009. Scaling properties and spatial organization of snow depth fields in sub-alpine forest and alpine tundra. Hydrol. Process. 23, 1575–1590.

Vermote, E., Justice, C., Claverie, M., Franch, B., 2016. Preliminary analysis of the performance of the landsat 8/OLI land surface reflectance product. Remote Sens. Environ. 185, 46–56. https://doi.org/10.1016/j.rse.2016.04.008.

Viviroli, D., Dürr, H.H., Messerli, B., Meybeck, M., Weingartner, R., 2007. Mountains of the world, water towers for humanity: typology, mapping, and global significance. Water Resources Res. 43, W07447. https://doi.org/10.1029/2006WR005653.

Winstral, A., Marks, D., 2002. Simulating wind fields and snow redistributions using terrain-based parameters to model accumulation and melt over a semi-arid mountain catchment. Hydrol. Process. 16, 3585–3603. https://doi.org/10.1002/hyp.1238.

Winstral, A., Elder, K., Davis, R.E., 2002. Spatial snow modeling of wind-redistributed snow using terrain-based parameters. J. Hydrometeorol. 3, 524–538.

Winstral, A., Marks, D., 2014. Long-term snow distribution observations in a mountain catchment: assessing variability, time stability, and the representativeness of an index site. Water Resources Res. 50, 293–305. https://doi.org/10.1002/2012WR013038.

Wrzesien, M.L., Durand, M.T., Pavelsky, T.M., Kapnick, S.B., Zhang, Y., Guo, J., Shum, C. K., 2018. A new estimate of north american mountain snow accumulation from regional cli- mate model simulations. Geophys. Res. Lett. 45, 1423–1432. https://doi.org/10.1002/2017GL076664.

Yang, J., Jiang, L., Luojus, K., Pan, J., Lemmetyinen, J., Takala, M., Wu, S., 2020. Snow depth estimation and historical data reconstruction over China based on a random forest machine learning approach. Cryosphere 14, 1763–1778. https://doi.org/10.5194/tc-14-1763-2020.

Zeller, L., McGrath, D., Sass, L., O'Neel, S., McNeil, C., Baker, E., 2022. Beyond glacier-wide mass balances: parsing seasonal elevation change into spatially-resolved patterns of accumulation and ablation at wolverine glacier. Alaska. J, Glaciol.